Acceleration of the hydrological cycle under global warming? An age-weighted regional water tagging approach

Jianhui Wei[1,*], Joël Arnault[1,2], Thomas Rummler[2], Benjamin Fersch[1], Zhenyu Zhang[1,2], Patrick Olschewski[1], Patrick Laux[1,2], Ningpeng Dong[3], Qianya Yang[4], Zikang Xing[5], Xin Li[6], Chuanguo Yang[7], Xuejun Zhang[8], Miaomiao Ma[8], Lu Gao[9], Ligang Xu[10], Zhongbo Yu[7], and Harald Kunstmann[1,2]

[1]Institute of Meteorology and Climate Research (IMK-IFU), Karlsruhe Institute of Technology, Campus Alpin, Garmisch-Partenkirchen, Germany

[2]Institute of Geography, Augsburg University, Augsburg, Germany

[3]Department of Water Resources, China Institute of Water Resources and Hydropower Research, Beijing, China

[4]Nanchang Institute of Technology, Nanchang, China

[5]College of Hydrology and Water Resources, Hohai University, Nanjing, China

[6]College of Water Conservancy and Hydropower Engineering, Hohai University, Nanjing, China

[7]State Key Laboratory of Hydrology-Water Resources and Hydraulic Engineering, Hohai University, Nanjing, China

[8]Research Center on Flood and Drought Disaster Reduction of the Ministry of Water Resources, China Institute of Water Resources and Hydropower Research, Beijing, China

[9]Institute of Geography, Fujian Normal University, Fuzhou, China

[10]Key Laboratory of Watershed Geographic Science, Nanjing Institute of Geography and Limnology, Chinese Academy of Sciences, Nanjing, China

[*]Corresponding author: Jianhui Wei (jianhui.wei@kit.edu) ORCID: 0000-0001-8609-9600

Abstract

Global warming is assumed to accelerate the global water cycle. However, quantification of the acceleration and regional analyses remain open. Accordingly, in this study we address the fundamental hydrological question: Is the water cycle regionally accelerating/decelerating under global warming? For our investigation we have implemented the age-weighted regional water tagging approach into the Weather Research and Forecasting WRF model, namely WRF-age, to follow the atmospheric water pathways and to derive atmospheric water residence times accordingly. Moreover, we have implemented the three-dimensional online budget analysis of the total, tagged, and aged atmospheric water into WRF-age to provide a prognostic equation of the atmospheric water residence times. The newly developed, physics-based WRF-age model is used to regionally downscale the reanalysis of ERA-Interim and the MPI-ESM Representative Concentration Pathway 8.5 scenario (RCP8.5) simulation exemplarily for an East Asian monsoon region, i.e., the Poyang Lake basin (the tagged moisture source area), for two 10-year slices of historical (1980-1989) and future (2040-2049) times. In comparison to the historical simulation, the future 2-meter temperature rises by +1.4 °C, evaporation increases by +6%, and precipitation decreases by -38% under RCP8.5 on average. In this context, global warming leads to regionally decreased residence times for the tagged water vapor by 8 hours and the tagged condensed moisture by 12 hours in the atmosphere, but increased transit times for the tagged precipitation by 4 hours over the land surface that is partly attributed to a slower fallout of precipitating moisture components in the atmosphere under global warming.

Keywords: Atmospheric water residence times, acceleration of the atmospheric hydrological cycle, the Weather Research and Forecasting model, age-weighted water tagging approach, East Asian monsoon region

Key Points

- Age-weighted water tagging approach is implemented into WRF to derive the atmospheric water residence time.
- 3-D online moisture budget analysis is extended in WRF for age-weighted atmospheric water to provide a prognostic equation of the atmospheric residence time.
- Global warming reduces the age of tagged water vapor and condensed moisture but increases the age of tagged precipitation over the Poyang Lake basin.

1. Introduction

It is well-accepted that global warming has been accelerating the global hydrological cycle (Held & Soden, 2006; Huntington, 2006; Olmedo et al., 2022; Yu et al., 2020), as concluded from observational findings (Huntington, 2006), theoretical expectations (Held & Soden, 2006), and modeling studies (Allen & Ingram, 2002). Accordingly, at the regional scale, such acceleration modifies weather regimes and increases the number of hydrometeorological extremes (Ficklin et al., 2019; Giorgi et al., 2011; Gu et al., 2023), thereby increasing the complexity of water resources management (Ficklin et al., 2022; Vahmani et al., 2022). Furthermore, continuous global warming in the future could also trigger multiple climate tipping points, which makes the changes (here, acceleration/deceleration) of the hydrological cycle at the regional scale and their associated impacts more complex (McKay et al., 2022; Blöschl et al., 2019; Lenton et al., 2008; Olschewski et al., 2023). Therefore, the understanding of regional hydrological cycle responses to global warming is fundamental to risk mitigation.

To quantify the acceleration/deceleration of the hydrological cycle, two types of approaches are often used: analytical methods with multiple datasets and numerical models with water-tracking techniques. For analytical methods, multiple indices are proposed to investigate the changes in the intensity of water fluxes in the hydrological cycle under global warming. For example, Giorgi et al. (2011) introduced the hydroclimatic intensity (HY-INT) index that synthesizes two metrics of precipitation intensity and dry spell length, with applications at regional and global scales (Giorgi et al., 2014; Mohan & Rajeevan, 2017). Huntington et al. (2018) presented the Water Cycle Intensity (WCI), which takes precipitation and actual evapotranspiration into

account, for quantifying the intensity of the hydrological cycle from a landscape point of view across multiple temporal scales. Recently, Ficklin et al. (2019) integrated precipitation surplus and evaporative demand, namely, the Surplus Deficit Intensity Index (SDI), to quantify hydrologic intensification by additionally accounting for changed atmospheric water demand under global warming. However, these indices can focus solely on changes in fluxes of water between terrestrial and atmosphere, which neglects atmospheric moisture transport, and in this case the acceleration/deceleration of the hydrological cycle can only be inferred.

A numerical model with water tracking techniques is an additional and more straightforward way to derive residence times of water in the atmosphere, i.e., a measure of the speed of the atmospheric hydrological cycle, and thereby evaluate changes in the speed and potential acceleration/deceleration of the hydrological cycle (van der Ent & Tuinenburg, 2017; Gimeno et al., 2021; Läderach & Sodemann, 2016; Trenberth, 1998; Tuinenburg & van der Ent, 2019; Wang et al., 2018; Wei et al., 2016). Here, the atmospheric water residence time is defined as the time between the original evaporation and the return of its respective water masses to the land surface as precipitation. Technically, moisture/particle tracking in numerical atmospheric models allows to characterize the pathways of evaporated and/or precipitating water with the consideration of atmospheric moisture transport and to diagnose the residence times of water vapor in the atmosphere (Bosilovich, 2002; Bosilovich et al., 2005; van der Ent et al., 2014; Läderach & Sodemann, 2016; Numaguti, 1999; Stohl & James, 2004; Wei et al., 2016). For example, Stohl & James (2004) implemented a Lagrangian analog to the Eulerian water budget analysis into the Lagrangian particle dispersion FLEXPART

model to derive the residence times in the total atmospheric column out of the meteorological analysis. Läderach & Sodemann (2016) further refined Lagrangian moisture source diagnostics and highlighted that simplified representations of moisture transport and precipitation processes in the tracking models lead to an overestimation of atmospheric moisture residence time globally. However, in FLEXPART, only the rate of change for the difference between evaporation and precipitation is diagnosed along trajectories, so that the respective impacts of evaporation and precipitation changes on the atmospheric moisture residence time cannot be disentangled (van der Ent & Tuinenburg, 2017). Recently, Tuinenburg & van der Ent (2019) extended the quasi-isentropic back-trajectory method of Dirmeyer & Brubaker (2007) to derive the probability density function of residence time of land evaporation on a global scale. Still, their model does not account for the vertical wind fields and neglects the vertical redistribution of the tracked parcel of water, which might introduce uncertainties in the derived patterns of the atmospheric residence time of water (Bosilovich, 2002; Goessling & Reick, 2013).

In addition to the Lagrangian framework, several Eulerian modeling frameworks have been proposed to estimate the residence time of atmospheric water in an offline calculation mode (van der Ent et al., 2014; Wang et al., 2018; Yoshimura et al., 2004). For example, the dynamic recycling model DRM (Wang et al., 2018) and the water account model WAM-2 Layers (Benedict et al., 2021; van der Ent et al., 2014; van der Ent et al., 2010; Wang-Erlandsson et al., 2018) take atmospheric analyses or model outputs, such as horizontal wind fields, specific humidity, surface pressure, precipitation, and evaporation, as their model inputs for forward-tracking of evaporation and

126 backward-tracking of precipitation. Accordingly, the atmospheric moisture residence
127 time increases linearly with time and is weighted by the updated tracked moisture during
128 model iteration at each time step. However, the two-dimensional field assumption does
129 not allow to account for three-dimensional effects such as wind shear and moist
130 convection (Goessling and Reick, 2013; van der Ent et al., 2013), and simple averaging
131 of estimates for different length scales and timescales may overlook the heterogeneity
132 of the land surface and the temporal variability (Bosilovich & Schubert, 2001; Trenberth,
133 1999).

134 To explicitly resolve the thermodynamical and precipitating processes and thus to
135 more realistically estimate the atmospheric moisture residence time, atmospheric online
136 models with the implementation of three-dimensional numerical water tagging
137 approaches have been used (Bosilovich et al., 2005; Bosilovich & Schubert, 2002; Wei
138 et al., 2016). In the last years, the numerical water tagging approaches have been
139 elaborated within regional climate models to investigate the moisture sources for
140 precipitation extremes and monsoon systems (Arnault et al., 2016; Dominguez et al.,
141 2016; Knoche & Kunstmann, 2013; Sodemann et al., 2009; Winschall et al., 2014).
142 Moreover, an “age-weighted” regional water tagging approach has been developed and
143 successfully implemented in one regional climate model (Wei et al., 2016). This
144 implementation allows for calculating residence times of atmospheric water states of
145 matter (i.e., different types of hydrometeors) and for diagnosing the speed of the
146 atmospheric branch of the hydrological cycle, which can be used to quantitatively
147 assess the regional effects of global warming-induced acceleration of the hydrological
148 cycle (Held & Soden, 2006; Huntington, 2006; Olmedo et al., 2022; Yu et al., 2020) in

more detail. Because of these advanced features, the RCM-derived highly accurate three-dimensional magnitude, location, and residence time of tagged atmospheric water states of matter have been often used to guide the future improvements of analytical methods for precipitation recycling studies, such as DRM (Dominguez et al., 2016) and WAM-2 Layer (van der Ent et al., 2013).

The land surface is characterized as highly heterogeneous concerning land cover, terrain height, and soil texture (Yates et al., 2003), and thereby interactions between the land surface and atmosphere are highly non-linear across scales (Betts et al., 1996; Wulfmeyer et al., 2018; Zhang et al., 2021). Over the last two decades, one of the Global Land Atmosphere System Study (GLASS) working groups (Hurk et al., 2011), namely, local coupling (LoCo) of land-atmosphere, promotes to develop processes-level, quantifiable metrics to diagnose the coupling among the land, planetary boundary layer, and precipitation (Santanello et al., 2018). However, the existing LoCo metrics listed in Santanello et al. (2018) have limited applicability in terms of investigated processes and temporal scales. Specifically, the process-based LoCo metrics summarized by Santanello et al. (2018), e.g., the concept of vector representation of heat and moisture budgets in the form of mixing diagrams (Milovac et al., 2016), do not apply to account for cloud formation and precipitating effect, and are not able to distinguish the local coupling of one specific region from other regions. To tackle the limitations of the existing LoCo metrics, the RCM-based regional water tagging approach is capable to quantify local land-atmosphere interactions by explicitly following atmospheric pathways of the water evaporated from a pre-defined region until it precipitates.

Using a RCM-based regional water tagging approach, the present study aims to address our hydrologically fundamental research question “Is the hydrological cycle regionally accelerating/decelerating under climate change?”, which has been ranked as the first out of the twenty-three unsolved problems in hydrology identified by the community process in 2018 (Blöschl et al., 2019). In particular, we present the newly developed WRF-age modeling system, that is the state-of-the-art Weather Research and Forecasting WRF model enhanced with the implementation of the age-weighted regional water tagging approach. For the case-study application, we choose to simulate and compare future and historical periods for the southeastern region of China, a region characterized by a monsoonal precipitation regime with a dry season during the winter months and a wet season during the summer months. It is reported that global warming may shift the position of this East Asian monsoonal circulation (Li et al., 2010; Li et al., 2023), which potentially generates droughts or floods in areas where this usually does not happen, thus affecting local economy (Hu et al., 2016). Recent studies also highlight that economic losses in China caused by warming-induced weather and climate extremes such as droughts, floods, and compound events might double between the 1.5 °C and 2.0 °C warming (Hao, 2022; Liu et al., 2022; Su et al., 2018).

The objectives of the present study are (1) to implement the age-weighted regional water tagging approach of Wei et al. (2016) and the three-dimensional online atmospheric water budget analysis of Arnault et al. (2016) into the Weather Research and Forecasting WRF modeling system, namely, the WRF-age, (2) to apply the WRF-age model to the Poyang Lake basin in the East Asian monsoon region for two 10-year slices of historical and future-warming times, and (3) to quantify to what extent the

regional atmospheric hydrological cycle is accelerated/decelerated under global warming.

2. Model and methodology

2.1. WRF with the age-weighted regional water tagging approach

The Weather Research and Forecast WRF model version 3.6.1 (Skamarock et al., 2008) is extended and employed for our accelerated/decelerated atmospheric hydrological cycle modeling study. WRF is a limited-area mesoscale model that simulates a coupled, nonlinear system of the soil, the vegetation, and the atmosphere. The WRF model has been employed for applications of, short-term weather forecasting (Gao et al., 2022; Yang et al., 2021), seasonal forecasts (Mori et al., 2020; Siegmund et al., 2015), historical climate simulations (Fersch & Kunstmann, 2014; Shang et al., 2022), and future climate projections (Wagner et al., 2013; Warrach-Sagi et al., 2013).

An evaporation tagging algorithm has been implemented in the WRF model version 3.5.1 by Arnault et al. (2016), with numerous applications for regions in Europe (Arnault et al., 2019), Africa (Arnault et al., 2021), and China (Shang et al., 2022; Zhang et al., 2019, 2022). This evaporation tagging algorithm is adapted to the WRF model version 3.6.1 used in this study, and further enhanced with the age-weighted evaporation tagging approach for regional climate models given by Wei et al. (2016). For the implementation of the age-weighted regional water tagging approach into the so-called WRF-age model, we closely follow our previous study in Wei et al. (2016). The age-weighted regional water tagging approach and the implementation strategy into regional climate models from Wei et al. (2016) has originally been developed with the

Fifth-Generation Pennsylvania State University/National Center for Atmospheric Research Mesoscale Model (MM5) version 3.5 (Dudhia, 1993; Grell et al., 1994).

The implementation of the age-weighted water tagging approach in WRF-age is summarized in three steps:

(1) Tagged evaporated water E_{tag} is calculated from a pre-defined moisture source area of the land surface by implementing a mask MASK_{tag} in the lower boundary condition of WRF;

$$E_{tag} = E \times \mathrm{MASK}_{tag} \quad (1)$$

$$\mathrm{MASK}_{tag} = \begin{cases} 1 & \text{for moisture source area} \\ 0 & \text{otherwise} \end{cases} \quad (2)$$

(2) The tagged water (Equation 3) and the age-weighted tagged water (Equation 4) are tracked until it returns to the land surface as precipitation by following the atmospheric water pathways. For this implementation, two additional equation sets for the tagged water states of matter $q_{k,tag}$ (kg kg^{-1}) and the age-weighted water states of matter $\tilde{q}_{k,tag}$(kg kg^{-1} s), describing three-dimensional grid-scale transport, horizontal *H* and vertical *V* subgrid-scale transport due to turbulence and diffusion *F*, phase change *C*, and the downward transport (namely, fallout) of precipitating water components *P*, are added to WRF-age. The subscript *k* denotes different types of hydrometeors.

$$\frac{\partial}{\partial t}\left(\mu \cdot q_{k,tag}\right) = \underbrace{-\left[\frac{\partial\left(\mu \cdot u \cdot q_{k,tag}\right)}{\partial x} + \frac{\partial\left(\mu \cdot v \cdot q_{k,tag}\right)}{\partial y} + \frac{\partial\left(\mu \cdot (g \cdot w - \Phi_x \cdot u - \Phi_y \cdot v) \cdot q_{k,tag}\right)}{\partial \eta}\right]}_{\text{Grid-scale transport}} + \underbrace{\mu \cdot \left(F^H_{q_{k,tag}} + F^V_{q_{k,tag}}\right)}_{\text{Subgrid-scale transport}} + \underbrace{\mu \cdot C_{q_{k,tag}}}_{\text{Phase change}} + \underbrace{\mu \cdot P_{q_{k,tag}}}_{\text{Fallout}} \quad (3)$$

$$\frac{\partial}{\partial t}(\mu \cdot \tilde{q}_{k,tag}) = \underbrace{-\left[\frac{\partial(\mu \cdot u \cdot \tilde{q}_{k,tag})}{\partial x} + \frac{\partial(\mu \cdot v \cdot \tilde{q}_{k,tag})}{\partial y} + \frac{\partial(\mu \cdot (g \cdot w - \Phi_x \cdot u - \Phi_y \cdot v) \cdot \tilde{q}_{k,tag})}{\partial \eta}\right]}_{\text{Grid-scale transport}} + \underbrace{\mu \cdot \left(F^H_{\tilde{q}_{k,tag}} + F^V_{\tilde{q}_{k,tag}}\right)}_{\text{Subgrid-scale transport}} + \underbrace{\mu \cdot C_{\tilde{q}_{k,tag}}}_{\text{Phase change}} + \underbrace{\mu \cdot P_{\tilde{q}_{k,tag}}}_{\text{Fallout}} + \underbrace{S_{\tilde{q}_{k,tag}}}_{\text{Advancing time}} \quad (4)$$

Here $\mu = P_{hs} - P_{ht}$ (Pa) represents the difference between the hydrostatic pressures at the top P_{ht} and surface P_{hs} of the model, which represents the mass of the dry air per unite area within the modeled atmospheric column. *x* (m) and *y* (m) denote the two horizontal coordinates. η (-) is the terrain-following hydrostatic pressure (mass) vertical coordinate. *u* (m s^{-1}), *v* (m s^{-1}), and *w* (m s^{-1}) are the two horizontal and vertical wind components. Φ (m^2 s^{-2}) is the geopotential and *g* (m s^{-2}) is the acceleration of gravity.

(3) Time weight information is included to the age-weighted tagged water due to atmospheric transport and phase change processes, in order to advance time for the age-weighted tagged water $\tilde{q}^{t+1}_{k,tag}$ at each model iteration as

$$\tilde{q}^{t+1}_{k,tag} = \tilde{q}^{t}_{k,tag} + \left(q^{t+1}_{k,tag} - q^{t}_{k,tag}\right) \times \Delta T, \quad (5)$$

where ΔT (s) denotes the model time step length and $\tilde{q}^{t}_{k,tag}$ denotes the preliminary age-weighed tagged moisture components from the previous model time step *t* due to time-weighted atmospheric transport and phase change.

2.2. Extension of the online budget analysis for age-weighted tagged water

In this study, we further extend the three-dimensional online atmospheric water budget analysis of Arnault et al. (2016) for age-weighted tagged water, thereby

providing a prognostic equation of the residence time of state variables in the atmospheric hydrological cycle.

The concept of the online budget analysis of atmospheric water states of matter is to compute the physical and dynamical tendencies of the model time step during model integration (Langhans, Fuhrer, et al., 2012). Such online budget analysis has been implemented into different regional climate models, such as the non-hydrostatic Consortium for Small-Scale Modeling (COSMO) model (Langhans, Schmidli, et al., 2012), the MM5 model (Braun, 2006), and the WRF model (Fita et al., 2019), for disentangling the precipitation generation mechanisms. In addition to the original atmospheric water states of matter, this approach has been extended by Arnault et al. (2016) for tagged atmospheric water states of matter (Equation 6) to understand the scale-dependency of regional precipitation recycling.

$$\begin{aligned}\left(dz \cdot \rho_d \cdot q_{k,tag}\right)_t = & \underbrace{dz \cdot \rho_d \cdot \mu^{-1} \cdot \left[-\frac{\partial\left(\mu \cdot u \cdot q_{k,tag}\right)}{\partial x} - \frac{\partial\left(\mu \cdot v \cdot q_{k,tag}\right)}{\partial y} + \mu \cdot F^H_{q_{k,tag}}\right]}_{\text{Horizontal transport}} \\ & \underbrace{+ dz \cdot \rho_d \cdot \mu^{-1} \cdot \left[-\frac{\partial\left(\mu \cdot (g \cdot w - \Phi_x \cdot u - \Phi_y \cdot v) \cdot \tilde{q}_{k,tag}\right)}{\partial \eta} + \mu \cdot F^V_{q_{k,tag}}\right]}_{\text{Vertical transport}} \\ & + \underbrace{dz \cdot \rho_d \cdot C_{q_{k,tag}}}_{\text{Phase change}} + \underbrace{dz \cdot \rho_d \cdot P_{q_{k,tag}}}_{\text{Fallout}}\end{aligned} \quad (6)$$

where dz (m) is the height step for a given model layer and ρ_d is the density of dry air.

In our WRF-age modeling environment, we use the online budget analysis of Equation 6 for tagged water and further extend this online budget analysis for age-weighted water. For this new extension, analogously to the implementation of the online budget analysis for tagged water in regional climate models described in Arnault et al. (2016), new variables representing budgets of the age-weighted tagged atmospheric

water states of matter are defined, and new diagnostic equations of Equation 7 integrating instantaneous values of the defined variables over space, height, and time are formulated in the source code of WRF. Terms of Equations 6 and 7 are integrated online at the time step of the model to provide a budget of tagged and age-weighted tagged atmospheric water states of matter, thereby allowing to calculate the atmospheric transit times of water.

$$\left(dz \cdot \rho_d \cdot \tilde{q}_{k,tag}\right)_t = \underbrace{dz \cdot \rho_d \cdot \mu^{-1} \cdot \left[-\frac{\partial\left(\mu \cdot u \cdot \tilde{q}_{k,tag}\right)}{\partial x} - \frac{\partial\left(\mu \cdot v \cdot \tilde{q}_{k,tag}\right)}{\partial y} + \mu \cdot F^{H}_{\tilde{q}_{k,tag}}\right]}_{\text{Horizontal transport}}$$

$$\underbrace{+\, dz \cdot \rho_d \cdot \mu^{-1} \cdot \left[-\frac{\partial\left(\mu \cdot (g \cdot w - \Phi_x \cdot u - \Phi_y \cdot v) \cdot \tilde{q}_{k,tag}\right)}{\partial \eta} + \mu \cdot F^{V}_{\tilde{q}_{k,tag}}\right]}_{\text{Vertical transport}} \tag{7}$$

$$+ \underbrace{dz \cdot \rho_d \cdot C_{\tilde{q}_{k,tag}}}_{\text{Phase change}} + \underbrace{dz \cdot \rho_d \cdot P_{\tilde{q}_{k,tag}}}_{\text{Fallout}} + \underbrace{S_{\tilde{q}_{k,tag}}}_{\text{Advancing time}}$$

2.3. Quantification of the atmospheric water pathways

The model extensions of section 2.1 and section 2.2 allow us to derive two categories of metrics to quantitatively understand the atmospheric water pathways, which are then employed to assess to what extent the regional atmospheric water cycle is accelerated/decelerated under global warming.

The contribution ratio ρ_W (%) is used to evaluate the strength of the land-atmosphere interaction. It quantifies to what extent the tagged water states of matter W_{tag} originating from a pre-defined moisture source region contributes to the total (original) water states of matter W in the atmospheric hydrological cycle:

$$\rho_W = W_{\text{tag}} / W_{\text{total}} \times 100 \tag{8}$$

279 W denotes arbitrary column-integrated variables, such as, water vapor q_v, condensed
280 atmospheric moisture q_d.

281 The atmospheric residence time τ_W (h) is defined as the age of tagged water
282 since its source (hereafter referred to as the age of water), evaluated with the ratio
283 between an age-weighted tagged variable and the corresponding tagged variable as

$$\tau_{W,tag} = \widetilde{W}_{tag}/W_{tag} \quad (9)$$

284 where $\widetilde{W}_{tag}$ denotes arbitrary column-integrated age-weighted tagged variables.

285 We further define the atmospheric transit time $T_{W,tag}$ (h) as the age of tagged
286 water since its source originating from a particular physical or dynamical process *pro*
287 (hereafter referred to as the age of water in flux), such as fallout and precipitation.

$$T_{W\_pro,tag} = \widetilde{W}_{pro,tag}/W_{pro,tag} \quad (10)$$

288

289 **3. The experimental design**

290 **3.1. Study area**

291 This WRF-age modeling study focuses on the Poyang Lake basin (Figure 1a)
292 with a spatial coverage of the basin of around 162,000 km^2 (Wei et al., 2021). The
293 topography of the basin varies from around 2000 m in the south to 50 m around the lake
294 area (Figure 1b). Poyang Lake, located in the northern part of the basin (29°N, 116°E),
295 is the largest freshwater lake in China. In a hydrological normal year, the area of the
296 lake is approximately 3,500 km^2 and the average depth of the lake is approximately 8.4
297 m (Feng et al., 2011). The land use in the Poyang Lake basin consists of forest (46%),
298 shrubland (25%), cropland (25%), and small areas of pasture, urban, and open water

(4%) (Ye et al., 2011; Zhang et al., 2014). The climate of the basin is categorized as a humid subtropical climate and has a strong seasonality of hot humid summers and cool dry winters (Wagner et al., 2016), which is mainly controlled by the East Asian monsoon (Ding & Chan, 2005; Xing et al., 2022; Zhang et al., 2011). The rainy season of the basin ranges from April to June and the summer is from June to August (Zhang et al., 2016). The mean annual basin-averaged 2-meter air temperature is around 17.5 °C, evaporation and precipitation are around 900 mm $year^{-1}$ and 1680 mm $year^{-1}$, respectively (Li & Zhang, 2011; Wei et al., 2015; Xing et al., 2022).

3.2. Domain setup and model configuration

For the domain setup and general model configuration of the newly developed WRF-age model, we closely follow the selection as chosen by Wei et al. (2015) and Wagner et al. (2016). A nested two-domain setup (Figure 1a) is used in this study. The first domain (D1) has a horizontal resolution of 30 km and an uneven vertical discretization of 38 layers up to 50 hPa for the atmosphere. The second domain (D2), centered over the Poyang Lake basin (Figure 1b), has a horizontal resolution of 5 km and 38 vertical layers of the atmosphere.

Table 1 lists the physical schemes of the WRF-age model applied in this study for both D1 and D2. They consist of the Dudhia scheme (Dudhia, 1989) for calculating shortwave radiation, the Rapid Radiation Transfer Model (RRTM) (Mlawer et al., 1997) for calculating longwave radiation, the WRF Single-Moment five-class scheme (WSM5) microphysics scheme (Hong et al., 2004), the Yonsei University (YSU) planetary boundary layer scheme (Hong et al., 2006), the Revised MM5 Monin-Obukhov surface layer scheme (Jiménez et al., 2012), the NOAH land surface model (Chen & Dudhia,

322 2001). For parameterizing cumulus, the Betts-Miller-Janjic (BMJ) scheme (Betts, 1986;
323 Betts & Miller, 1986; Janjić, 2002) is applied only for the outer domain D1. The model
324 setup and the physical schemes selected in this study have been intensively evaluated
325 and widely used in our previous studies of regional climate modeling for the Poyang
326 Lake basin (Wagner et al., 2013; Wagner et al., 2016; Wei et al., 2015, 2016).

327 For the WRF-age setup, the moisture source area of the Earth's land surface
328 focused on in this study is the Poyang Lake basin (light blue shaded area in Figure 1a),
329 from which the evaporated water is "tagged, tracked, and aged" when entering the
330 atmosphere. To separate the moisture source of the Poyang Lake basin from the
331 surrounding, a pre-defined mask (with values of 1 for the Poyang Lake basin and of 0
332 for otherwise, Equations 1 and 2) is added into the static boundary condition of WRF-
333 age for D2. Then, the tagged and age-weighted water undergo the same dynamic and
334 physical processes of the atmosphere as the original atmospheric water states of matter,
335 until they return to the land surface of D2 as tagged and age-weighted tagged
336 precipitation or leave the D2 model domain.

337 **3.3. Simulation protocol**

338 In this study, two regional dynamical downscaling simulations using the newly
339 developed WRF-age model are conducted: (1) a control simulation for historical periods
340 (CTRL) and (2) a warming scenario simulation under Representative Concentration
341 Pathway 8.5 for future periods (RCP8.5), which corresponds to the atmospheric carbon
342 dioxide concentration being in the range of 851-1379 ppm by 2100. All two simulations
343 are carried out for the East Asian monsoon region for an 11-year slice. The first year of

two simulations is selected as the model spin-up time and the remaining 10 years of the simulations are used for the warming-induced acceleration/deceleration analysis.

For the CTRL simulation, the initial and lateral boundary conditions to drive the WRF-age model are taken from the European Centre for Medium Range Weather Forecasts Interim reanalysis (Dee et al., 2011). The CTRL simulation is initialized on January 1st, 1979 at 0000 UTC and covers the historical period 1979-1989. For the RCP8.5 simulation, the Max-Planck-Institute Earth System Model (MPI-ESM) RCP8.5 scenario (Giorgetta et al., 2013) is dynamically downscaled using WRF-age for the future period 2039-2049.

Regarding the selection of the emission scenario RCP8.5, this is because that, for our investigation future period 2040-2049, the changes in the projected temperature and precipitation over South China under RCP4.5 follows those under RCP8.5, with relatively fewer deviations in comparison with these during far future periods, e.g., 2090-2100 (Gu et al., 2015). On the other hand, our selection of the high-emission RCP8.5 warming scenario referred to as “business-as-usual” facilitates the elaboration of the accelerated atmospheric hydrological cycle under global warming.

MPI-ESM is selected because the changes in the projected precipitation and temperature over South China by the MPI models are most similar to those derived from the multiple model ensemble of CMIP5 (Gu et al., 2015), and latest CMIP6 models (You et al., 2021; Zhang et al., 2022). Therefore, it is expected that our WRF-age downscaled MIP-ESM future projection over the Poyang Lake basin is in agreement with the robust regional climate change signals derived from the multiple model ensemble.

366 To quantitively assess the warming-induced alternations of the regional
367 atmospheric water cycle, we denote

$$\Delta(\cdot) = (\cdot)_{\mathrm{RCP8.5}} - (\cdot)_{\mathrm{CTRL}} \quad (11)$$

368 where subscripts “RCP8.5” and “CTRL” indicate the values of an arbitrary quantity in
369 parentheses during the future warming period and the historical period.

370 **3.4. Reference data and evaluation strategy**

371 To evaluate the performance of the basic WRF model in reproducing the
372 historical climate of the study region, the simulated 2-meter air temperature *T2*,
373 evaporation *E*, and precipitation *P* from the CTRL simulation are compared to gridded
374 reference datasets. For *T2* and *P*, the CN05.1 product released by China
375 Meteorological Administration is used. It provides daily gridded temperature and
376 precipitation estimates over China since 1961 at a horizontal resolution of 0.25° (Wu &
377 Gao, 2013). CN05.1 is derived by spatially interpolating records collected from around
378 2416 meteorological stations in China. For *E*, the satellite- and reanalysis-based Global
379 Land Evaporation Amsterdam Methodology (GLEAM) version 3.6a product is chosen.
380 GLEAM provides daily gridded global evaporation estimates for the period 1980-2021 at
381 a 0.25° × 0.25° spatial resolution (Martens et al., 2017). Relative to the previous version
382 3.3, the upgraded version 3.6a is derived by additionally merging the latest reanalysis
383 ERA5 and by updating to the latest version of input data sets (e.g., precipitation, soil
384 moisture) using the revised approaches for calculating evaporative stress, optimizing
385 drainage, and assimilating soil moisture (Martens et al., 2017). The reference datasets
386 selected in this study have been widely used for validating regional climate simulations

(e.g., Shang et al., 2022) and for studying climate changes (e.g., Shang et al., 2021) in East Asian monsoon regions.

For comparison of the simulations to the reference data, the bilinear interpolation method is employed to remap the simulated variables of the WRF grids to the respective reference data grids. Three statistical metrics, namely, mean error *ME*, mean relative error *MRE* (%), and Pearson's correlation coefficient *r* (-) with a calculated *p*-value (here the significance level of 99% is employed), are used to quantify the performance of the WRF model in terms of reproducing spatial patterns and temporal variations of *T2*, *E*, and *P* of the reference:

$$ME = \sum_{t=1}^{t=N} (SIM_t - REF_t) \tag{12}$$

$$MRE = \frac{\sum_{t=1}^{t=N} (SIM_t - REF_t)}{\sum_{t=1}^{t=N} REF_t} \times 100\% \tag{13}$$

$$r = \frac{\sum_{t=1}^{t=N} (SIM_t - \overline{SIM})(REF_t - \overline{REF})}{\sqrt{\sum_{t=1}^{t=N} (SIM_t - \overline{SIM})^2} \sqrt{\sum_{t=1}^{t=N} (REF_t - \overline{REF})^2}} \tag{14}$$

where SIM_t and REF_t denote the simulated and reference variable at the t^{th} time step of evaluation, respectively. *N* is the total number of time steps of evaluation. $\overline{SIM}$ and $\overline{REF}$ denote the spatial (temporal) mean of the simulated and reference variables for the evaluation of spatial pattern (temporal variation), respectively.

4. Results and discussion

In this section, we investigate the warming-altered regional water cycle by comparing the WRF-age downscaled RCP8.5 simulation with CTRL simulation, concerning land

surface process, atmospheric water pathways, land-atmosphere interactions, and atmospheric water residence times.

4.1. Evaluation of simulated T2, E, and P

Figure 2 shows the spatial distributions of *T2*, *E,* and *P* derived from the reference datasets (left column) and the WRF simulation (middle column) for the Poyang Lake basin averaged for 1980-1989, and the corresponding differences in the spatial patterns (right column). Figure 3 compares the monthly variations of the basin-averaged, simulated *T2*, *E*, and *P* to the reference data from 1980 to 1989.

For *T2*, the observed pattern of higher temperatures over the central and southern parts of the basin (Figure 2a) is well reproduced by the simulation (Figure 2b), with very minor cold biases (*ME* = -0.4 °C, in Figure 2c). The monthly variation in the simulated basin-averaged *T2* matches well with the variation of the observation (r = 0.99; p-value < 0.01), although slightly cold biases over the basin are found in summer (Figure 3a).

For *E*, the higher evaporation rates (> 1.8 mm day^{-1}) over the lake area and in the western (southern) from the reference data are well reproduced by the WRF model with slight overestimations (underestimations), except for the low-land region where the observed lower evaporation rates are much overestimated (RME = +20%, Figure 2d-2f). Temporally, the WRF model can reproduce the observed monthly variation in the basin-averaged *E* (r = 0.95; p-value < 0.01), particularly for the months from August to April (Figure 3b). Moreover, it is found that overestimated *E* during the rainy season (May-July) is coherent with the overestimated *P* during the same period (compare Figure 3b and Figure 3c).

For *P*, the WRF model can reproduce higher (relatively smaller) precipitation rates over the eastern (mid-western) part of the basin, despite observed high precipitation rates (> 5 mm day^{-1}) being much overestimated (*ME* = +43%, Figure 2g-2i). Figure 3c depicts that the basin-averaged monthly variation in *P* has a good agreement with that derived from the reference data (r = 0.88; p-value < 0.01), especially the periodic characteristics in *P* associated with the development of the East Asian summer monsoon. Considerable overestimation of the observed precipitation is found only for the months when maximum rainfall occurs. Such overestimation of *P* is also found in WRF-based convection-permitting simulations of warm-season *P* over East China (Yun et al., 2020), although comparatively higher spatial resolution and different physical schemes have been applied. Yun et al. (2020) attributed the WRF overestimated heavy precipitation over mountainous South China to the inappropriate treatment of sub-grid cloud fraction and the lack of representation of aerosol effects. On a short temporal scale, Zhu et al. (2018) focused on evaluating 48-hour WRF forecasts of precipitation over China during the 2013-2014 summer season. They reported that the WRF model overpredicts afternoon convections near Southeast China, which is likely due to deficiencies in the representation of certain physical processes related to precipitation in WRF (e.g., Surcel et al., 2010).

Nevertheless, it is argued that our WRF model setup provides state-of-the-art results and can realistically reproduce the climatological characteristics of the East-Asian monsoon-controlled Poyang Lake basin, which encourages us to investigate the alterations of land surface processes and atmospheric water pathways due to global warming with the WRF-age model using this setup.

449 **4.2. Warming-altered land-surface processes**

450 In this section, we investigate the warming-altered land-surface processes for our
451 study region by spatially and temporally comparing the WRF-downscaled future RCP8.5
452 simulation with the WRF-downscaled historical CTRL simulation for *T2*, *E*, and *P*, as
453 shown in Figure 4.

454 Figure 4a shows the spatial pattern of the simulated 10-year averaged *T2* in
455 CTRL, displaying that the values of *T2* in the southern part of the basin are higher than
456 those in the northern part. In comparison to CTRL, the projected 10-year averaged *T2* in
457 RCP8.5 increases by around +0.5 °C in the southern part of the basin and by around
458 +1.5 °C in the northern part (Figure 4b). Such increases in basin-averaged *T2* are found
459 throughout the entire year, especially for March, April, and December (> 3 °C), and the
460 highest monthly *T2* shifts from July in CTRL to August in RCP8.5 (Figure 4c).
461 The spatial pattern of the simulated 10-year averaged *E* in CTRL shows that the
462 maximum *E* is found over the lake area (Figure 4d). In comparison to CTRL, the
463 warming enhances the evaporation processes noticeably over the lake area and slightly
464 over the southern part of the basin, whereas the decreased *E* is pronounced in the
465 areas surrounding the lake (Figure 4e). On the monthly scale, the warming-induced
466 enhancement in *E* becomes larger from November to August, with a decreased *E* in
467 May, September, and October (Figure 4f). The largest monthly *E* shifts from July in
468 CTRL to June in RCP8.5.

469 The comparison of the simulated *P* in RCP8.5 with that in CTRL demonstrates
470 that decreases in *P* are projected for the whole Poyang Lake basin (Figure 4h) and all

months except for December when minimal rainfall happens (Figure 4i). Moreover, the monthly variation in the basin-averaged *P* in RCP8.5 is projected to be lower.

Averaged over the basin and over the 10-year time slices, the comparison of RCP8.5 to CTRL shows that global warming leads to increased *T2* by +1.4 °C, slightly enhanced *E* by +6%, and noticeably decreased *P* by -38% for the Poyang Lake basin. Such warmer and drier changes for the Poyang Lake basin have been reported in studies about assessment of regional climate change by evaluating products of multiple global climate models (Lu et al., 2021; Zhang et al., 2022) and multiple regional climate models (Gu et al., 2018). For example, Gu et al. (2018) compared the five RCMs downscaled regional climate over China during 2030-2049 under RCP4.5 to those during the reference historical period 1980-1999. They found that, under RCP4.5, the WRF-projected future changes in temperature and precipitation over Southern China including our study region is +0.5 °C and -15%, which agrees with the sign of changes found in this study. Recent research activities about the assessment of climate change over China under the Coupled Models Intercomparison Project Phase 6 (CMIP6) multiple scenarios confirm that the future climate for the Poyang Lake basin will continuously warm up and become drier in the future (Tian et al., 2021; You et al., 2021; Zhang et al., 2022). As for land evaporation, Lu et al. (2021) evaluated and assessed 16 CMIP6 model simulations under three scenarios for China. They found that the land evaporation over the humid region including the Poyang Lake basin during the projection period 2020-2099 shows significant positive trends in comparison to that during the baseline period 1995-2014, which is in line with our finding of the enhanced land evaporation for the Poyang Lake basin under RCP8.5.

4.3. Warming-altered atmospheric water pathways

To quantitively understand the warming-altered regional atmospheric cycle, the analysis of the atmospheric water pathways with the age-weighted regional water tagging approach (Equation 6) is performed. The RCP8.5 and CTRL WRF-age derived quantities of column-integrated tagged water vapor $W_{qv,tag}$, column-integrated tagged condensed atmospheric moisture $W_{qd,tag}$, and tagged precipitation P_{tag}, that are originating from the evaporated water from the Poyang Lake basin, in RCP8.5 are compared spatially and temporally, as shown in Figure 5.

Figure 5a shows the spatial pattern of the 10-year averaged column-integrated tagged water vapor $W_{qv,tag}$ over the Poyang Lake basin in CTRL, displaying that larger amounts of the evaporated water (> 0.7 mm) exist over the southeastern part of the basin. In comparison to CTRL, the atmosphere over the Poyang Lake basin in RCP8.5 holds more tagged water vapor $W_{qv,tag}$ (Figure 5b), in accordance with the increased *T2* (Figures 4a-4c) and the warming enhanced *E* (Figures 4d-4f). On the monthly scale, the increases in $W_{qv,tag}$ in RCP8.5 are larger during the warmer and rainy months (March-August) and become negligible during October-December (Figure 5c).

The spatial pattern of the 10-year averaged column-integrated tagged condensed atmospheric moisture $W_{qd,tag}$ shown in Figure 5d provides information about clouds and precipitation formation. In comparison to CTRL, warming in RCP8.5 leads to more $W_{qd,tag}$ over the northern part of the basin (Figure 5e), and during the rainy period from April to August (Figure 5f). On the contrary, warming in RCP8.5 leads to less $W_{qd,tag}$ in the atmosphere from September to January (Figure 5f).

516 The comparison of the 10-year averaged tagged precipitation P_{tag} shows that
517 warming in RCP8.5 results in decreased P_{tag} over the basin (Figure 5h). Such
518 decreased P_{tag} in RCP8.5 is projected in nearly every month of the investigated years
519 (Figure 5i).

520 Averaged over the basin and over the 10-year time slices, the atmosphere over
521 the Poyang Lake basin in RCP8.5 will hold more tagged water vapor $W_{qv,tag}$ by +66%,
522 form more tagged clouds $W_{qd,tag}$ by 41%, but generate less tagged precipitation by -83%
523 in comparison to CTRL.

524 **4.4. Warming-altered land-atmosphere interactions**

525 The impact of global warming on the land-atmosphere interactions is quantitively
526 assessed by spatially and temporally comparing the multiple-year averaged contribution
527 ratios $\rho_{qv,tag}$, $\rho_{qd,tag}$, and $\rho_{P,tag}$ (Equation 8) in RCP8.5 with ones in CTRL, as shown in
528 Figure 6.

529 Figure 6a depicts the spatial pattern of the 10-year averaged contribution ratio
530 $\rho_{qv,tag}$ for the column-integrated tagged water vapor $W_{qv,tag}$ in CTRL, revealing that the
531 evaporated water from the Poyang Lake basin has higher contribution (> 3%) to the
532 total water vapor over the western part of the basin and relatively lower contribution (<
533 1%) over the eastern part. In comparison to CTRL, the contribution ratio $\rho_{qv,tag}$ in
534 RCP8.5 is increased by around +3% over the middle-western part of the basin and has
535 no changes over the eastern border of the basin (Figure 6b). Temporally, warming leads
536 to higher increases (+2%) in the contribution ratio $\rho_{qv,tag}$ from February to June, and
537 such increases become less from July to November (Figure 6c)

538 The spatial pattern of $\rho_{qd,tag}$ in Figure 6d shows that in CTRL the contribution
539 ratio of the tagged condensed atmospheric moisture $W_{qd,tag}$ to the total condensed
540 moisture W_{qd} reaches the highest values (> 3%) over the southwestern part of the
541 basin. In comparison to CTRL (Figure 6e), warming leads to increased contribution
542 ratios $\rho_{qd,tag}$ with the highest increases over the area of the lake (+3%). Temporally, the
543 contribution ratios $\rho_{qd,tag}$ in RCP8.5 are higher than those in CTRL from February to
544 August but lower from September to January (Figure 6f).

545 Figure 6g reveals that the contribution $\rho_{P,tag}$ of the evaporated water to the
546 precipitation over the same basin in CTRL is around 3.5%, with the highest values (5%)
547 over the eastern part adjacent to the lake area and the southern part where the
548 mountainous regions are. In comparison to CTRL, the contribution ratio $\rho_{P,tag}$ in
549 RCP8.5 decreases over the entire basin (Figure 6h), and throughout the whole year
550 (Figure 6i).

551 Averaged over the basin and over the 10-year time slices, the comparison of
552 RCP8.5 to CTRL suggests that global warming will slightly strengthen the land-
553 atmosphere interactions with respect to water vapor (by +2%) and clouds (by +1%), but
554 will weaken the interactions with respect to precipitation (by -1%).

555 **4.5. Warming-altered speed of the atmospheric water cycle**

556 The impact of global warming on the speed of the atmospheric water cycle is
557 quantitively assessed by spatially and temporally comparing the multiple-year averaged
558 atmospheric residence time $\tau_{qv,tag}$, $\tau_{qd,tag}$ (Equation 9) and atmospheric transit time
559 $T_{P,tag}$ (Equation 10) in RCP8.5 with these in CTRL, as shown in Figure 7.

Figure 7a shows the spatial pattern of the 10-year averaged atmospheric residence times $\tau_{qv,tag}$ in CTRL, displaying that the evaporated water from the Poyang Lake basin stays short (~15 hours) in the atmosphere particularly over the lowland lake and its southwestern surroundings (see Figure 1b), and stays longer (> 22 hours) over relatively high-elevation mountainous region (see Figure 1b). In comparison to CTRL, the atmospheric residence times $\tau_{qv,tag}$ in RCP8.5 are projected to be shorter (Figure 7b). The monthly variation in $\tau_{qv,tag}$ in RCP8.5 becomes larger than that in CTRL (Figure 7c), and the shortest atmospheric residence times $\tau_{qv,tag}$ are found in October-December in RCP8.5 (around 10 hours), but in July in CTRL (around 15 hours).

The spatial pattern of the 10-year averaged atmospheric residence times $\tau_{qd,tag}$ in CTRL (Figure 7d) shows that in general the larger amount of the column-integrated tagged condensed moisture $W_{qd,tag}$ (> 0.003 mm shown in Figure 5d) has shorter atmospheric residence time (< 24 hours), whereas the smaller amount of $W_{qd,tag}$ (< 0.002 mm in Figure 5d) has longer atmospheric residence time (> 28 hours). In comparison to CTRL, warming in RCP8.5 leads to shorter atmospheric residence times $\tau_{qd,tag}$ over the entire basin and also changed spatial distributions of $\tau_{qd,tag}$, i.e., shorter (longer) $\tau_{qd,tag}$ over the eastern (western) part of the basin (Figure 7e). Temporally, warming in RCP8.5 increases the monthly variation in $\tau_{qd,tag}$, and the atmospheric residence times $\tau_{qd,tag}$ in RCP8.5 becomes shorter (longer) during the period September-April (May-August) than these in CTRL (Figure 7f).

Regarding the spatial patterns of $T_{P,tag}$, the tagged precipitation in CTRL has shorter (longer) atmospheric transit times over the southern (northwestern) part of the

basin (Figure 7g). In comparison to CTRL, the similar pattern of $T_{P,tag}$ in RCP8.5 is found, but with an increased magnitude of $T_{P,tag}$ and increased corresponding spatial variation (Figure 7h). Temporally, warming in RCP8.5 increases the atmospheric transit times $T_{P,tag}$ and decreases the temporal variation in $T_{P,tag}$ than these in CTRL (Figure 7i). The periodic characteristic of $T_{P,tag}$ in CTRL, that is lower values of $T_{P,tag}$ from early summer to early autumn and higher values of $T_{P,tag}$ from late autumn to early spring, still exist in RCP8.5, except for two additional months (October and November) with lower values of $T_{P,tag}$ in RCP8.5.

Averaged over the basin and over the 10-year time slices, the comparison of RCP8.5 to CTRL suggests that global warming will shorten the residence times of the tagged water vapor by 8 hours and the tagged condensed moisture by 12 hours in the atmosphere, but will prolong the transit times of the tagged precipitation by 4 hours over the land surface, for the Poyang Lake basin.

To understand the contrasting results of the acceleration of the tagged clouds in the atmosphere (Figure 7d-f) and the deceleration of the tagged precipitation over the land surface (Figure 7g-i), we further derive the atmosphere transit time of the column-integrated tagged condensed atmospheric moisture due to fallout $T_{qd\_fallout,tag}$ (see Equations 6 and 7), as shown in Figure 8. It is worth noting that, as the WSM5 microphysics scheme is used in this study, the tagged condensed atmospheric moisture (Figure 5d) consists of the non-precipitating tagged liquid water substance (cloud droplets), non-precipitating solid water substance (cloud ice particles), *precipitating* liquid water substance (rain droplets), and *precipitating* solid water substance (snowflakes and other solid forms). The tagged condensed atmospheric moisture due to

fallout provides information about the precipitating moisture components only. It is found that the spatial pattern of the atmospheric transit time $T_{qd\_fallout,tag}$ in CTRL (Figure 8a) is similar to that of the tagged precipitation (Figure 7g). In comparison to CTRL, warming leads to increased $T_{qd\_fallout,tag}$ in the eastern part of the basin and decreased in the western part (Figure 8b). Temporally, warming results in increased $T_{qd\_fallout,tag}$ from March to September and decreased $T_{qd\_fallout,tag}$ from October to January (Figure 8c), which is consistent with the warming-included changes in $T_{P,tag}$ (Figure 7i). Such consistent temporal variations of $T_{qd\_fallout,tag}$ and $T_{P,tag}$ reveal that global warming will modify the precipitating regime over the Poyang Lake basin: Under global warming, the fallout of precipitating moisture components in the atmosphere will take more time, thereby resulting in increased $T_{P,tag}$ over the land surface.

6. Summary and Conclusions

This study presents the newly developed WRF-age model, that is the Weather Research and Forecasting WRF model of Skamarock et al. (2008) with the implementations of the age-weighed regional water tagging approach from Wei et al. (2016) and the online moisture budget analysis of Arnault et al. (2016) extended for the aged-weighted water. The new model allows us to follow the atmospheric water pathways, to derive atmospheric water residence times, i.e., a measure of the speed of the atmospheric water cycle, and to provide a prognostic equation of the atmospheric water residence times. The WRF-age model has been used to dynamically downscale the reanalysis of ERA-Interim and the MPI-ESM RCP8.5 scenario simulation for the Poyang Lake basin, for two 10-year time slices of past (1980-1989) and future (2040-

627 2049) climate. In these WRF-age simulations, the Poyang Lake basin is chosen as the
628 source of tagged moisture for the age tracing algorithm. The contribution ratio, the
629 residence time of atmospheric water states of matter, and the corresponding
630 atmospheric transit time have been employed to quantitatively assess the regionally
631 accelerated/decelerated atmospheric hydrological cycle under global warming.

632 In comparison to the historical WRF-age simulation, the 2-meter air temperature
633 rises on average by +1.4 °C, evaporation increases by +6%, and precipitation
634 decreases by -38% in the future under RCP8.5. In this context, global warming will
635 shorten the residence times of the tagged water vapor by 8 hours and the tagged
636 condensed moisture by 12 hours in the atmosphere, but will prolong the transit times of
637 the tagged precipitation by 4 hours over the land surface that is in agreement with the
638 reduced land precipitation amounts. Such prolonged atmospheric transit time of land
639 precipitation under global warming is partly attributed to a slower fallout of precipitating
640 moisture components in the atmosphere under global warming. We also found that
641 global warming will lead to slightly increased contributions of the evaporation to the
642 water vapor and the condensed atmospheric moisture over the Poyang Lake basin, but
643 slightly decreased contributions of the evaporation to the precipitation. These distinct,
644 warming-induced changes in the contribution ratios suggest that global warming will
645 alter the local land-atmosphere interactions over the Poyang Lake basin.

646 This first study with WRF-age demonstrates the potential of this model for
647 deriving the residence times of atmospheric water states of matter, with the
648 considerations of three-dimensional physical and thermodynamical processes in the
649 atmosphere and the interactions of land-atmosphere. Moreover, our warming-induced

acceleration findings demonstrate that global warming increases the complexity of the regional atmospheric hydrological cycle, especially the associated changes in the speed of atmospheric water states of matter. Overall, it is concluded that our modeling study confirms the acceleration of the regional atmospheric water cycle under global warming, except for the precipitation-related processes. Our findings enhance the understanding of the warming-induced acceleration/deceleration of the atmospheric hydrological cycle at regional scales.

Despite the above-mentioned advanced features of our newly developed WRF-age model, one potential limitation of our RCM-based age-weighted regional water tagging approach is that the model-derived results of tracked evaporated water and respective atmospheric residence times depend on how realistically an RCM can simulate all the relevant processes of terrestrial hydrology, vegetation, and atmosphere (Gimeno et al., 2012). Direct validation of our model-derived results would be possible by tracking the water isotopologues as done in, e.g., Arnault, Jung, et al. (2021) and Arnault et al. (2022).

Acknowledgments

This research was supported through funding of the AccHydro (KU 2090/11-1) and COSMIC-SENSE (FOR2694, KU 2090/12-2) projects by the German Research Foundation, the National Natural Science Foundation of China (41761134090), the MitRiskFlood (01LP2005A) and SALDi (01LL1701B) projects by the German Federal Ministry of Science of Education, and the LANDKLIF project which is sponsored by the Bavarian State Ministry of Science and the Arts in the context of the Bavarian Climate Research Network (bayklif). Qianya Yang is supported financially by the Natural

673 Science Foundation of Jiangxi Province (No.20224BAB214080). The authors would like
674 to thank the following data sources: The CN05.1 product is available from the China
675 Meteorological Administration. The GLEAM ET product is available from
676 https://www.gleam.eu. Model developments and simulations were conducted on the
677 high-performance computing (HPC) system at KIT/IMK-IFU. We thank the IT Team at
678 KIT/IMK-IFU for the HPC support.

679 **References**

680 Allen, M. R., & Ingram, W. J. (2002). Constraints on future changes in climate and the
681 hydrologic cycle. *Nature*, *419*(6903), 224–32. https://doi.org/10.1038/nature01092
682 Armstrong McKay, D. I., Staal, A., Abrams, J. F., Winkelmann, R., Sakschewski, B., Loriani, S.,
683 et al. (2022). Exceeding 1.5°C global warming could trigger multiple climate tipping
684 points. *Science*, *377*(6611), eabn7950. https://doi.org/10.1126/science.abn7950
685 Arnault, Joel, Knoche, R., Wei, J., & Kunstmann, H. (2016a). Evaporation tagging and
686 atmospheric water budget analysis with WRF: A regional precipitation recycling study
687 for West Africa. *Water Resources Research*, *52*(3), 1544–1567.
688 https://doi.org/10.1002/2015WR017704
689 Arnault, Joel, Knoche, R., Wei, J., & Kunstmann, H. (2016b). Evaporation tagging and
690 atmospheric water budget analysis with WRF: A regional precipitation recycling study
691 for West Africa. *Water Resources Research*, *52*(3), 1544–1567.
692 https://doi.org/10.1002/2015WR017704
693 Arnault, Joël, Wei, J., Rummler, T., Fersch, B., Zhang, Z., Jung, G., et al. (2019). A Joint Soil-
694 Vegetation-Atmospheric Water Tagging Procedure With WRF-Hydro: Implementation
695 and Application to the Case of Precipitation Partitioning in the Upper Danube River

Basin. *Water Resources Research*, *55*(7), 6217–6243. https://doi.org/10.1029/2019WR024780

Arnault, Joël, Jung, G., Haese, B., Fersch, B., Rummler, T., Wei, J., et al. (2021). A Joint Soil-Vegetation-Atmospheric Modeling Procedure of Water Isotopologues: Implementation and Application to Different Climate Zones With WRF-Hydro-Iso. *Journal of Advances in Modeling Earth Systems*, *13*(10), e2021MS002562. https://doi.org/10.1029/2021MS002562

Arnault, Joël, Fersch, B., Rummler, T., Zhang, Z., Quenum, G. M., Wei, J., et al. (2021). Lateral terrestrial water flow contribution to summer precipitation at continental scale – A comparison between Europe and West Africa with WRF-Hydro-tag ensembles. *Hydrological Processes*, *35*(5). https://doi.org/10.1002/hyp.14183

Arnault, Joël, Niezgoda, K., Jung, G., Hahn, A., Zabel, M., Schefuß, E., & Kunstmann, H. (2022). Disentangling the Contribution of Moisture Source Change to Isotopic Proxy Signatures: Deuterium Tracing with WRF-Hydro-Iso-Tag and Application to Southern African Holocene Sediment Archives. *Journal of Climate*, *35*(22), 3855–3879. https://doi.org/10.1175/JCLI-D-22-0041.1

Benedict, I., van Heerwaarden, C. C., van der Linden, E. C., Weerts, A. H., & Hazeleger, W. (2021). Anomalous moisture sources of the Rhine basin during the extremely dry summers of 2003 and 2018. *Weather and Climate Extremes*, *31*, 100302. https://doi.org/10.1016/j.wace.2020.100302

Betts, A. K. (1986). A new convective adjustment scheme. Part I: Observational and theoretical basis. *Quarterly Journal of the Royal Meteorological Society*. https://doi.org/10.1002/qj.49711247307

719 Betts, A. K., & Miller, M. J. (1986). A new convective adjustment scheme. Part II: Single
720 column tests using GATE wave, BOMEX, ATEX and arctic air-mass data sets. *Quarterly*
721 *Journal of the Royal Meteorological Society*. https://doi.org/10.1002/qj.49711247308
722 Betts, Alan K., Ball, J. H., Beljaars, A. C. M., Miller, M. J., & Viterbo, P. A. (1996). The land
723 surface-atmosphere interaction: A review based on observational and global modeling
724 perspectives. *Journal of Geophysical Research*, *101*(D3), 7209.
725 https://doi.org/10.1029/95JD02135
726 Blöschl, G., Bierkens, M. F. P., Chambel, A., Cudennec, C., Destouni, G., Fiori, A., et al. (2019).
727 Twenty-three unsolved problems in hydrology (UPH) – a community perspective.
728 *Hydrological Sciences Journal*, *64*(10), 1141–1158.
729 https://doi.org/10.1080/02626667.2019.1620507
730 Bosilovich, M. G. (2002). On the vertical distribution of local and remote sources of water for
731 precipitation. *Meteorology and Atmospheric Physics*, *80*(1–4), 31–41.
732 https://doi.org/10.1007/s007030200012
733 Bosilovich, Michael G., & Schubert, S. D. (2001). Precipitation Recycling over the Central
734 United States Diagnosed from the GEOS-1 Data Assimilation System. *Journal of*
735 *Hydrometeorology*, *2*(1), 26–35. https://doi.org/10.1175/1525-
736 7541(2001)002<0026:PROTCU>2.0.CO;2
737 Bosilovich, Michael G, & Schubert, S. D. (2002). Water Vapor Tracers as Diagnostics of the
738 Regional Hydrologic Cycle. *Journal of Hydrometeorology*, *3*(2), 149–165.
739 https://doi.org/10.1175/1525-7541(2002)003<0149:WVTADO>2.0.CO;2

740 Bosilovich, Michael G., Schubert, S. D., & Walker, G. K. (2005). Global Changes of the Water
741 Cycle Intensity. *Journal of Climate*, *18*(10), 1591–1608.
742 https://doi.org/10.1175/JCLI3357.1
743 Braun, S. A. (2006). High-Resolution Simulation of Hurricane Bonnie (1998). Part II: Water
744 Budget. *Journal of the Atmospheric Sciences*, *63*(1), 43–64.
745 https://doi.org/10.1175/JAS3609.1
746 Chen, F., & Dudhia, J. (2001). Coupling an Advanced Land Surface–Hydrology Model with the
747 Penn State–NCAR MM5 Modeling System. Part I: Model Implementation and
748 Sensitivity. *Monthly Weather Review*, *129*(4), 569–585. https://doi.org/10.1175/1520-
749 0493(2001)129<0587:CAALSH>2.0.CO;2
750 Dee, D. P., Uppala, S. M., Simmons, A. J., Berrisford, P., Poli, P., Kobayashi, S., et al. (2011).
751 The ERA-Interim reanalysis: configuration and performance of the data assimilation
752 system. *Quarterly Journal of the Royal Meteorological Society*, *137*(656), 553–597.
753 https://doi.org/10.1002/qj.828
754 Ding, Y., & Chan, J. C. L. (2005). The East Asian summer monsoon: an overview. *Meteorology*
755 *and Atmospheric Physics*, *89*(1–4), 117–142. https://doi.org/10.1007/s00703-005-0125-z
756 Dirmeyer, P. A., & Brubaker, K. L. (2007). Characterization of the Global Hydrologic Cycle
757 from a Back-Trajectory Analysis of Atmospheric Water Vapor. *Journal of*
758 *Hydrometeorology*, *8*(1), 20–37. https://doi.org/10.1175/JHM557.1
759 Dominguez, F., Miguez-Macho, G., & Hu, H. (2016). WRF with Water Vapor Tracers: A Study
760 of Moisture Sources for the North American Monsoon. *Journal of Hydrometeorology*,
761 *17*(7), 1915–1927. https://doi.org/10.1175/JHM-D-15-0221.1

762 Dudhia, J. (1989). Numerical Study of Convection Observed during the Winter Monsoon
763 Experiment Using a Mesoscale Two-Dimensional Model. *Journal of the Atmospheric*
764 *Sciences*, *46*(20), 3077–3107. https://doi.org/10.1175/1520-
765 0469(1989)046<3077:NSOCOD>2.0.CO;2
766 Dudhia, J. (1993). A Nonhydrostatic Version of the Penn State–NCAR Mesoscale Model:
767 Validation Tests and Simulation of an Atlantic Cyclone and Cold Front. *Monthly*
768 *Weather Review*, *121*(5), 1493–1513. https://doi.org/10.1175/1520-
769 0493(1993)121<1493:ANVOTP>2.0.CO;2
770 van der Ent, R. J., Tuinenburg, O. A., Knoche, H.-R., Kunstmann, H., & Savenije, H. H. G.
771 (2013). Should we use a simple or complex model for moisture recycling and
772 atmospheric moisture tracking? *Hydrology and Earth System Sciences*, *17*(12), 4869–
773 4884. https://doi.org/10.5194/hess-17-4869-2013
774 van der Ent, R. J., Wang-Erlandsson, L., Keys, P. W., & Savenije, H. H. G. (2014). Contrasting
775 roles of interception and transpiration in the hydrological cycle – Part 2: Moisture
776 recycling. *Earth System Dynamics*, *5*(2), 471–489. https://doi.org/10.5194/esd-5-471-
777 2014
778 van der Ent, Rudi J., Savenije, H. H. G., Schaefli, B., & Steele-Dunne, S. C. (2010). Origin and
779 fate of atmospheric moisture over continents. *Water Resources Research*, *46*(9), n/a-n/a.
780 https://doi.org/10.1029/2010WR009127
781 van der Ent, Ruud J., & Tuinenburg, O. A. (2017). The residence time of water in the atmosphere
782 revisited. *Hydrology and Earth System Sciences*, *21*(2), 779–790.
783 https://doi.org/10.5194/hess-21-779-2017

784 Feng, L., Hu, C., Chen, X., Li, R., Tian, L., & Murch, B. (2011). MODIS observations of the
785 bottom topography and its inter-annual variability of Poyang Lake. *Remote Sensing of*
786 *Environment*, *115*(10), 2729–2741. https://doi.org/10.1016/j.rse.2011.06.013
787 Fersch, B., & Kunstmann, H. (2014). Atmospheric and terrestrial water budgets: sensitivity and
788 performance of configurations and global driving data for long term continental scale
789 WRF simulations. *Climate Dynamics*, *42*(9–10), 2367–2396.
790 https://doi.org/10.1007/s00382-013-1915-5
791 Ficklin, D. L., Abatzoglou, J. T., & Novick, K. A. (2019). A New Perspective on Terrestrial
792 Hydrologic Intensity That Incorporates Atmospheric Water Demand. *Geophysical*
793 *Research Letters*, *46*(14), 8114–8124. https://doi.org/10.1029/2019GL084015
794 Ficklin, D. L., Null, S. E., Abatzoglou, J. T., Novick, K. A., & Myers, D. T. (2022).
795 Hydrological Intensification Will Increase the Complexity of Water Resource
796 Management. *Earth's Future*, *10*(3), e2021EF002487.
797 https://doi.org/10.1029/2021EF002487
798 Fita, L., Polcher, J., Giannaros, T. M., Lorenz, T., Milovac, J., Sofiadis, G., et al. (2019).
799 CORDEX-WRF v1.3: development of a module for the Weather Research and
800 Forecasting (WRF) model to support the CORDEX community. *Geoscientific Model*
801 *Development*, *12*(3), 1029–1066. https://doi.org/10.5194/gmd-12-1029-2019
802 Gao, L., Wei, J., Lei, X., Ma, M., Wang, L., Guan, X., & Lin, H. (2022). Simulation of an
803 Extreme Precipitation Event Using Ensemble-Based WRF Model in the Southeastern
804 Coastal Region of China. *Atmosphere*, *13*(2), 194.
805 https://doi.org/10.3390/atmos13020194

Gimeno, L., Stohl, A., Trigo, R. M., Dominguez, F., Yoshimura, K., Yu, L., et al. (2012). Oceanic and terrestrial sources of continental precipitation. *Reviews of Geophysics*, *50*(4), RG4003. https://doi.org/10.1029/2012RG000389

Gimeno, L., Eiras-Barca, J., Durán-Quesada, A. M., Dominguez, F., van der Ent, R., Sodemann, H., et al. (2021). The residence time of water vapour in the atmosphere. *Nature Reviews Earth & Environment*, *2*(8), 558–569. https://doi.org/10.1038/s43017-021-00181-9

Giorgetta, M. A., Jungclaus, J., Reick, C. H., Legutke, S., Bader, J., Böttinger, M., et al. (2013). Climate and carbon cycle changes from 1850 to 2100 in MPI-ESM simulations for the Coupled Model Intercomparison Project phase 5. *Journal of Advances in Modeling Earth Systems*, *5*(3), 572–597. https://doi.org/10.1002/jame.20038

Giorgi, F., Im, E.-S., Coppola, E., Diffenbaugh, N. S., Gao, X. J., Mariotti, L., & Shi, Y. (2011). Higher Hydroclimatic Intensity with Global Warming. *Journal of Climate*, *24*(20), 5309–5324. https://doi.org/10.1175/2011JCLI3979.1

Giorgi, F., Coppola, E., & Raffaele, F. (2014). A consistent picture of the hydroclimatic response to global warming from multiple indices: Models and observations. *Journal of Geophysical Research: Atmospheres*, *119*(20), 11,695-11,708. https://doi.org/10.1002/2014JD022238

Goessling, H. F., & Reick, C. H. (2013). On the "well-mixed" assumption and numerical 2-D tracing of atmospheric moisture. *Atmospheric Chemistry and Physics*, *13*(11), 5567–5585. https://doi.org/10.5194/acp-13-5567-2013

Grell, A. G., Dudhia, J., & Stauffer, R. D. (1994). *A description of the fifth-generation Penn State/NCAR Mesoscale Model (MM5)*. https://doi.org/10.5065/D60Z716B

828 Gu, H., Yu, Z., Wang, J., Wang, G., Yang, T., Ju, Q., et al. (2015). Assessing CMIP5 general
829 circulation model simulations of precipitation and temperature over China. *International*
830 *Journal of Climatology*, *35*(9), 2431–2440. https://doi.org/10.1002/joc.4152
831 Gu, H., Yu, Z., Yang, C., Ju, Q., Yang, T., & Zhang, D. (2018). High-resolution ensemble
832 projections and uncertainty assessment of regional climate change over China in
833 CORDEX East Asia. *Hydrology and Earth System Sciences*, *22*(5), 3087–3103.
834 https://doi.org/10.5194/hess-22-3087-2018
835 Gu, L., Yin, J., Slater, L. J., Chen, J., Do, H. X., Wang, H.-M., et al. (2023). Intensification of
836 Global Hydrological Droughts Under Anthropogenic Climate Warming. *Water Resources*
837 *Research*, *59*(1), e2022WR032997. https://doi.org/10.1029/2022WR032997
838 Hao, Z. (2022). Compound events and associated impacts in China. *IScience*, *25*(8), 104689.
839 https://doi.org/10.1016/j.isci.2022.104689
840 Held, I. M., & Soden, B. J. (2006). Robust Responses of the Hydrological Cycle to Global
841 Warming. *Journal of Climate*, *19*(21), 5686–5699. https://doi.org/10.1175/JCLI3990.1
842 Hong, S.-Y., Dudhia, J., & Chen, S.-H. (2004). A Revised Approach to Ice Microphysical
843 Processes for the Bulk Parameterization of Clouds and Precipitation. *Monthly Weather*
844 *Review*, *132*(1), 103–120. https://doi.org/10.1175/1520-
845 0493(2004)132<0103:ARATIM>2.0.CO;2
846 Hong, S.-Y., Noh, Y., Dudhia, J., Hong, S.-Y., Noh, Y., & Dudhia, J. (2006). A New Vertical
847 Diffusion Package with an Explicit Treatment of Entrainment Processes. *Monthly*
848 *Weather Review*, *134*(9), 2318–2341. https://doi.org/10.1175/MWR3199.1

Hu, X., Hall, J. W., Shi, P., & Lim, W. H. (2016). The spatial exposure of the Chinese infrastructure system to flooding and drought hazards. *Natural Hazards*, *80*(2), 1083–1118. https://doi.org/10.1007/s11069-015-2012-3

Huntington, T. G. (2006). Evidence for intensification of the global water cycle: Review and synthesis. *Journal of Hydrology*, *319*(1–4), 83–95. https://doi.org/10.1016/j.jhydrol.2005.07.003

Huntington, T. G., Weiskel, P. K., Wolock, D. M., & McCabe, G. J. (2018). A new indicator framework for quantifying the intensity of the terrestrial water cycle. *Journal of Hydrology*, *559*, 361–372. https://doi.org/10.1016/j.jhydrol.2018.02.048

Hurk, B. van den, Best, M., Dirmeyer, P., Pitman, A., Polcher, J., & Santanello, J. (2011). Acceleration of Land Surface Model Development over a Decade of Glass. *Bulletin of the American Meteorological Society*, *92*(12), 1593–1600. https://doi.org/10.1175/BAMS-D-11-00007.1

Janjić, Z. I. (2002). Comments on "Development and Evaluation of a Convection Scheme for Use in Climate Models." *Journal of the Atmospheric Sciences*. https://doi.org/10.1175/1520-0469(2000)057<3686:codaeo>2.0.co;2

Jiménez, P. A., Dudhia, J., González-Rouco, J. F., Navarro, J., Montávez, J. P., & García-Bustamante, E. (2012). A Revised Scheme for the WRF Surface Layer Formulation. *Monthly Weather Review*, *140*(3), 898–918. https://doi.org/10.1175/mwr-d-11-00056.1

Knoche, H. R., & Kunstmann, H. (2013). Tracking atmospheric water pathways by direct evaporation tagging: A case study for West Africa. *Journal of Geophysical Research: Atmospheres*, *118*(22), 12,345-12,358. https://doi.org/10.1002/2013JD019976

871 Läderach, A., & Sodemann, H. (2016). A revised picture of the atmospheric moisture residence
872 time. *Geophysical Research Letters*. https://doi.org/10.1002/2015GL067449
873 Langhans, W., Schmidli, J., Schär, C., Langhans, W., Schmidli, J., & Schär, C. (2012). Bulk
874 Convergence of Cloud-Resolving Simulations of Moist Convection over Complex
875 Terrain. *Journal of the Atmospheric Sciences*, *69*(7), 2207–2228.
876 https://doi.org/10.1175/JAS-D-11-0252.1
877 Langhans, W., Fuhrer, O., & Schmidli, J. (2012). Description and application of a budget
878 diagnosis tool in COSMO. In *COSMO Newsletter* (p. No. 12, 43-51).
879 Lenton, T. M., Held, H., Kriegler, E., Hall, J. W., Lucht, W., Rahmstorf, S., & Schellnhuber, H.
880 J. (2008). Tipping elements in the Earth's climate system. *Proceedings of the National*
881 *Academy of Sciences*, *105*(6), 1786–1793. https://doi.org/10.1073/pnas.0705414105
882 Li, J., Wu, Z., Jiang, Z., & He, J. (2010). Can Global Warming Strengthen the East Asian
883 Summer Monsoon? *Journal of Climate*, *23*(24), 6696–6705.
884 https://doi.org/10.1175/2010JCLI3434.1
885 Li, Xianghu, & Zhang, Q. (2011). Estimating the Potential Evapotranspiration of Poyang Lake
886 Basin Using Remote Sense Data and Shuttleworth-Wallace Model. *Procedia*
887 *Environmental Sciences*, *10*, 1575–1582. https://doi.org/10.1016/j.proenv.2011.09.250
888 Li, Xin, Fang, G., Wei, J., Arnault, J., Laux, P., Wen, X., & Kunstmann, H. (2023). Evaluation
889 and projection of precipitation and temperature in a coastal climatic transitional zone in
890 China based on CMIP6 GCMs. *Climate Dynamics*. https://doi.org/10.1007/s00382-023-
891 06781-z

Liu, L., Gao, J., & Wu, S. (2022). Warming of 0.5 °C may cause double the economic loss and increase the population affected by floods in China. *Natural Hazards and Earth System Sciences*, *22*(5), 1577–1590. https://doi.org/10.5194/nhess-22-1577-2022

Lu, J., Wang, G., Li, S., Feng, A., Zhan, M., Jiang, T., et al. (2021). Projected Land Evaporation and Its Response to Vegetation Greening Over China Under Multiple Scenarios in the CMIP6 Models. *Journal of Geophysical Research: Biogeosciences*, *126*(9), e2021JG006327. https://doi.org/10.1029/2021JG006327

Martens, B., Miralles, D. G., Lievens, H., van der Schalie, R., de Jeu, R. A. M., Fernández-Prieto, D., et al. (2017). GLEAM v3: satellite-based land evaporation and root-zone soil moisture. *Geoscientific Model Development*, *10*(5), 1903–1925. https://doi.org/10.5194/gmd-10-1903-2017

Milovac, J., Warrach-Sagi, K., Behrendt, A., Späth, F., Ingwersen, J., & Wulfmeyer, V. (2016). Investigation of PBL schemes combining the WRF model simulations with scanning water vapor differential absorption lidar measurements. *Journal of Geophysical Research: Atmospheres*, *121*(2), 624–649. https://doi.org/10.1002/2015JD023927

Mlawer, E. J., Taubman, S. J., Brown, P. D., Iacono, M. J., & Clough, S. A. (1997). Radiative transfer for inhomogeneous atmospheres: RRTM, a validated correlated-k model for the longwave. *Journal of Geophysical Research*, *102*(D14), 16663. https://doi.org/10.1029/97JD00237

Mohan, T. S., & Rajeevan, M. (2017). Past and future trends of hydroclimatic intensity over the Indian monsoon region. *Journal of Geophysical Research: Atmospheres*, *122*(2), 896–909. https://doi.org/10.1002/2016JD025301

914 Mori, P., Schwitalla, T., Ware, M. B., Warrach-Sagi, K., & Wulfmeyer, V. (2020). Downscaling
915 of seasonal ensemble forecasts to the convection-permitting scale over the Horn of Africa
916 using the WRF model. *International Journal of Climatology*.
917 https://doi.org/10.1002/joc.6809
918 Numaguti, A. (1999). Origin and recycling processes of precipitating water over the Eurasian
919 continent: Experiments using an atmospheric general circulation model. *Journal of*
920 *Geophysical Research*, *104*(D2), 1957. https://doi.org/10.1029/1998JD200026
921 Olmedo, E., Turiel, A., González-Gambau, V., González-Haro, C., García-Espriu, A., Gabarró,
922 C., et al. (2022). Increasing stratification as observed by satellite sea surface salinity
923 measurements. *Scientific Reports*, *12*(1), 6279. https://doi.org/10.1038/s41598-022-
924 10265-1
925 Olschewski, P., Laux, P., Wei, J., Böker, B., Tian, Z., Sun, L., & Kunstmann, H. (2023). An
926 ensemble-based assessment of bias adjustment performance, changes in
927 hydrometeorological predictors and compound extreme events in EAS-CORDEX.
928 *Weather and Climate Extremes*, *39*, 100531. https://doi.org/10.1016/j.wace.2022.100531
929 Santanello, J. A., Dirmeyer, P. A., Ferguson, C. R., Findell, K. L., Tawfik, A. B., Berg, A., et al.
930 (2018). Land-atmosphere interactions the LoCo perspective. *Bulletin of the American*
931 *Meteorological Society*. https://doi.org/10.1175/BAMS-D-17-0001.1
932 Shang, S., Zhu, G., Wei, J., Li, Y., Zhang, K., Li, R., et al. (2021). Associated Atmospheric
933 Mechanisms for the Increased Cold Season Precipitation over the Three-River
934 Headwaters Region from the Late 1980s. *Journal of Climate*, *34*(19), 8033–8046.
935 https://doi.org/10.1175/JCLI-D-21-0077.1

936 Shang, S., Arnault, J., Zhu, G., Chen, H., Wei, J., Zhang, K., et al. (2022). Recent Increase of
937 Spring Precipitation over the Three-River Headwaters Region—Water Budget Analysis
938 Based on Global Reanalysis (ERA5) and ET-Tagging Extended Regional Climate
939 Modeling. *Journal of Climate*, *35*(22), 3599–3617. https://doi.org/10.1175/JCLI-D-21-
940 0829.1
941 Siegmund, J., Bliefernicht, J., Laux, P., & Kunstmann, H. (2015). Toward a seasonal
942 precipitation prediction system for West Africa: Performance of CFSv2 and high-
943 resolution dynamical downscaling. *Journal of Geophysical Research: Atmospheres*,
944 *120*(15), 7316–7339. https://doi.org/10.1002/2014JD022692
945 Singh, H. A., Bitz, C. M., Nusbaumer, J., & Noone, D. C. (2016). A mathematical framework for
946 analysis of water tracers: Part 1: Development of theory and application to the
947 preindustrial mean state. *Journal of Advances in Modeling Earth Systems*, *8*(2), 991–
948 1013. https://doi.org/10.1002/2016MS000649
949 Singh, H. K. A., Bitz, C. M., Donohoe, A., Nusbaumer, J., & Noone, D. C. (2016). A
950 Mathematical Framework for Analysis of Water Tracers. Part II: Understanding Large-
951 Scale Perturbations in the Hydrological Cycle due to CO2 Doubling. *Journal of Climate*,
952 *29*(18), 6765–6782. https://doi.org/10.1175/JCLI-D-16-0293.1
953 Skamarock, W., Klemp, J., Dudhia, J., Gill, D., Barker, D., Wang, W., et al. (2008). A
954 Description of the Advanced Research WRF Version 3. *NCAR Technical Note*
955 *NCAR/TN-475+STR*. https://doi.org/10.5065/D68S4MVH
956 Sodemann, H., Wernli, H., & Schwierz, C. (2009). Sources of water vapour contributing to the
957 Elbe flood in August 2002-A tagging study in a mesoscale model. *Quarterly Journal of*
958 *the Royal Meteorological Society*, *135*(638), 205–223. https://doi.org/10.1002/qj.374

959 Stohl, A., & James, P. (2004). A Lagrangian Analysis of the Atmospheric Branch of the Global
960 Water Cycle. Part I: Method Description, Validation, and Demonstration for the August
961 2002 Flooding in Central Europe. *Journal of Hydrometeorology*, *5*(4), 656–678.
962 https://doi.org/10.1175/1525-7541(2004)005<0656:ALAOTA>2.0.CO;2
963 Su, B., Huang, J., Fischer, T., Wang, Y., Kundzewicz, Z. W., Zhai, J., et al. (2018). Drought
964 losses in China might double between the 1.5 °C and 2.0 °C warming. *Proceedings of the*
965 *National Academy of Sciences*, *115*(42), 10600–10605.
966 https://doi.org/10.1073/pnas.1802129115
967 Surcel, M., Berenguer, M., & Zawadzki, I. (2010). The Diurnal Cycle of Precipitation from
968 Continental Radar Mosaics and Numerical Weather Prediction Models. Part I:
969 Methodology and Seasonal Comparison. *Monthly Weather Review*, *138*(8), 3084–3106.
970 https://doi.org/10.1175/2010MWR3125.1
971 Tian, J., Zhang, Z., Ahmed, Z., Zhang, L., Su, B., Tao, H., & Jiang, T. (2021). Projections of
972 precipitation over China based on CMIP6 models. *Stochastic Environmental Research*
973 *and Risk Assessment*, *35*(4), 831–848. https://doi.org/10.1007/s00477-020-01948-0
974 Trenberth, K. E. (1998). Atmospheric Moisture Residence Times and Cycling: Implications for
975 Rainfall Rates and Climate Change. *Climatic Change*, *39*(4), 667–694.
976 https://doi.org/10.1023/A:1005319109110
977 Trenberth, K. E. (1999). Atmospheric Moisture Recycling: Role of Advection and Local
978 Evaporation. *Journal of Climate*, *12*(5), 1368–1381. https://doi.org/10.1175/1520-
979 0442(1999)012<1368:AMRROA>2.0.CO;2

980 Tuinenburg, O. A., & van der Ent, R. J. (2019). Land Surface Processes Create Patterns in
981 Atmospheric Residence Time of Water. *Journal of Geophysical Research: Atmospheres*,
982 *124*(2), 583–600. https://doi.org/10.1029/2018JD028871
983 Vahmani, P., Jones, A. D., & Li, D. (2022). Will Anthropogenic Warming Increase
984 Evapotranspiration? Examining Irrigation Water Demand Implications of Climate
985 Change in California. *Earth's Future*, *10*(1), e2021EF002221.
986 https://doi.org/10.1029/2021EF002221
987 Wagner, S., Fersch, B., Kunstmann, H., Yuan, F., Yang, C., & Yu, Z. (2013).
988 Hydrometeorological modelling for Poyang Lake region, China. *IAHS-AISH Publication*,
989 *359*, 152–157.
990 Wagner, Sven, Berg, P., Schädler, G., & Kunstmann, H. (2013). High resolution regional climate
991 model simulations for Germany: Part II-projected climate changes. *Climate Dynamics*.
992 https://doi.org/10.1007/s00382-012-1510-1
993 Wagner, Sven, Fersch, B., Yuan, F., Yu, Z., & Kunstmann, H. (2016). Fully coupled
994 atmospheric-hydrological modeling at regional and long-term scales: Development,
995 application, and analysis of WRF-HMS. *Water Resources Research*, *52*(4), 3187–3211.
996 https://doi.org/10.1002/2015WR018185
997 Wang, N., Zeng, X.-M., Zheng, Y., Zhu, J., & Jiang, S. (2018). The Atmospheric Moisture
998 Residence Time and Reference Time for Moisture Tracking over China. *Journal of*
999 *Hydrometeorology*, *19*(7), 1131–1147. https://doi.org/10.1175/JHM-D-17-0204.1
1000 Wang-Erlandsson, L., Fetzer, I., Keys, P. W., van der Ent, R. J., Savenije, H. H. G., & Gordon,
1001 L. J. (2018). Remote land use impacts on river flows through atmospheric

1002 teleconnections. *Hydrology and Earth System Sciences*, *22*(8), 4311–4328.
1003 https://doi.org/10.5194/hess-22-4311-2018
1004 Warrach-Sagi, K., Schwitalla, T., Wulfmeyer, V., & Bauer, H.-S. (2013). Evaluation of a climate
1005 simulation in Europe based on the WRF–NOAH model system: precipitation in
1006 Germany. *Climate Dynamics*, *41*(3–4), 755–774. https://doi.org/10.1007/s00382-013-
1007 1727-7
1008 Wei, J., Knoche, H. R., & Kunstmann, H. (2015). Contribution of transpiration and evaporation
1009 to precipitation: An ET-Tagging study for the Poyang Lake region in Southeast China.
1010 *Journal of Geophysical Research: Atmospheres*, *120*(14), 6845–6864.
1011 https://doi.org/10.1002/2014JD022975
1012 Wei, J., Knoche, H. R., & Kunstmann, H. (2016). Atmospheric residence times from
1013 transpiration and evaporation to precipitation: An age-weighted regional evaporation
1014 tagging approach. *Journal of Geophysical Research: Atmospheres*, *121*(12), 6841–6862.
1015 https://doi.org/10.1002/2015JD024650
1016 Wei, J., Dong, N., Fersch, B., Arnault, J., Wagner, S., Laux, P., et al. (2021). Role of reservoir
1017 regulation and groundwater feedback in a simulated ground-soil-vegetation continuum: A
1018 long-term regional scale analysis. *Hydrological Processes*, *35*(8), e14341.
1019 https://doi.org/10.1002/hyp.14341
1020 Winschall, A., Pfahl, S., Sodemann, H., & Wernli, H. (2014). Comparison of Eulerian and
1021 Lagrangian moisture source diagnostics – the flood event in eastern Europe in May 2010.
1022 *Atmospheric Chemistry and Physics*, *14*(13), 6605–6619. https://doi.org/10.5194/acp-14-
1023 6605-2014

1024 Wu, J., & Gao, X. (2013). A gridded daily observation dataset over China region and comparison
1025 with the other datasets. *Chinese Journal of Geophysics*, *56*(4), 1102–1111.
1026 https://doi.org/10.6038/cjg20130406
1027 Wulfmeyer, V., Turner, D. D., Baker, B., Banta, R., Behrendt, A., Bonin, T., et al. (2018). A
1028 New Research Approach for Observing and Characterizing Land-Atmosphere Feedback.
1029 *Bulletin of the American Meteorological Society*, BAMS-D-17-0009.1.
1030 https://doi.org/10.1175/BAMS-D-17-0009.1
1031 Xing, Z., Yu, Z., Wei, J., Zhang, X., Ma, M., Yi, P., et al. (2022). Lagged influence of ENSO
1032 regimes on droughts over the Poyang Lake basin, China. *Atmospheric Research*, *275*,
1033 106218. https://doi.org/10.1016/j.atmosres.2022.106218
1034 Yang, Q., Yu, Z., Wei, J., Yang, C., Gu, H., Xiao, M., et al. (2021). Performance of the WRF
1035 model in simulating intense precipitation events over the Hanjiang River Basin, China –
1036 A multi-physics ensemble approach. *Atmospheric Research*.
1037 https://doi.org/10.1016/j.atmosres.2020.105206
1038 Yates, D. N., Chen, F., & Nagai, H. (2003). Land Surface Heterogeneity in the Cooperative
1039 Atmosphere Surface Exchange Study (CASES-97). Part II: Analysis of Spatial
1040 Heterogeneity and Its Scaling. *Journal of Hydrometeorology*, *4*(2), 219–234.
1041 https://doi.org/10.1175/1525-7541(2003)4<219:LSHITC>2.0.CO;2
1042 Ye, X., Zhang, Q., Bai, L., & Hu, Q. (2011). A modeling study of catchment discharge to
1043 Poyang Lake under future climate in China. *Quaternary International*, *244*(2), 221–229.
1044 https://doi.org/10.1016/j.quaint.2010.07.004

1045 Yoshimura, K., Oki, T., Ohte, N., & Kanae, S. (2004). Colored Moisture Analysis Estimates of
1046 Variations in 1998 Asian Monsoon Water Sources. *Journal of the Meteorological Society*
1047 *of Japan*, *82*(5), 1315–1329. https://doi.org/10.2151/jmsj.2004.1315
1048 You, Q., Cai, Z., Wu, F., Jiang, Z., Pepin, N., & Shen, S. S. P. (2021). Temperature dataset of
1049 CMIP6 models over China: evaluation, trend and uncertainty. *Climate Dynamics*, *57*(1),
1050 17–35. https://doi.org/10.1007/s00382-021-05691-2
1051 Yu, L., Josey, S. A., Bingham, F. M., & Lee, T. (2020). Intensification of the global water cycle
1052 and evidence from ocean salinity: a synthesis review. *Annals of the New York Academy of*
1053 *Sciences*, *1472*(1), 76–94. https://doi.org/10.1111/nyas.14354
1054 Yun, Y., Liu, C., Luo, Y., Liang, X., Huang, L., Chen, F., & Rasmmusen, R. (2020).
1055 Convection-permitting regional climate simulation of warm-season precipitation over
1056 Eastern China. *Climate Dynamics*, *54*(3), 1469–1489. https://doi.org/10.1007/s00382-
1057 019-05070-y
1058 Zhang, M., Xu, W., Hu, Z., Merz, C., Ma, M., Wei, J., et al. (2022). Projection of future climate
1059 change in the Poyang Lake Basin of China under the global warming of 1.5–3°C.
1060 *Frontiers in Environmental Science*, *10*. Retrieved from
1061 https://www.frontiersin.org/articles/10.3389/fenvs.2022.985145
1062 Zhang, Qi, Ye, X., Werner, A. D., Li, Y., Yao, J., Li, X., & Xu, C. (2014). An investigation of
1063 enhanced recessions in Poyang Lake: Comparison of Yangtze River and local catchment
1064 impacts. *Journal of Hydrology*, *517*, 425–434.
1065 https://doi.org/10.1016/j.jhydrol.2014.05.051

1066 Zhang, Qiang, Liu, Y., Yang, G., & Zhang, Z. (2011). Precipitation and hydrological variations
1067 and related associations with large-scale circulation in the Poyang Lake basin, China.
1068 *Hydrological Processes*, *25*(5), 740–751. https://doi.org/10.1002/hyp.7863
1069 Zhang, Qiang, Xiao, M., Singh, V. P., & Wang, Y. (2016). Spatiotemporal variations of
1070 temperature and precipitation extremes in the Poyang Lake basin, China. *Theoretical and*
1071 *Applied Climatology*. https://doi.org/10.1007/s00704-015-1470-6
1072 Zhang, Z., Arnault, J., Wagner, S., Laux, P., & Kunstmann, H. (2019). Impact of Lateral
1073 Terrestrial Water Flow on Land-Atmosphere Interactions in the Heihe River Basin in
1074 China: Fully Coupled Modeling and Precipitation Recycling Analysis. *Journal of*
1075 *Geophysical Research: Atmospheres*, *124*(15), 8401–8423.
1076 https://doi.org/10.1029/2018JD030174
1077 Zhang, Z., Arnault, J., Laux, P., Ma, N., Wei, J., & Kunstmann, H. (2021). Diurnal cycle of
1078 surface energy fluxes in high mountain terrain: High-resolution fully coupled
1079 atmosphere-hydrology modelling and impact of lateral flow. *Hydrological Processes*,
1080 *35*(12), e14454. https://doi.org/10.1002/hyp.14454
1081 Zhang, Z., Arnault, J., Laux, P., Ma, N., Wei, J., Shang, S., & Kunstmann, H. (2022).
1082 Convection-permitting fully coupled WRF-Hydro ensemble simulations in high mountain
1083 environment: impact of boundary layer- and lateral flow parameterizations on land–
1084 atmosphere interactions. *Climate Dynamics*, *59*(5), 1355–1376.
1085 https://doi.org/10.1007/s00382-021-06044-9
1086 Zhu, K., Xue, M., Zhou, B., Zhao, K., Sun, Z., Fu, P., et al. (2018). Evaluation of Real-Time
1087 Convection-Permitting Precipitation Forecasts in China During the 2013–2014 Summer

1088 Season. *Journal of Geophysical Research: Atmospheres*, *123*(2), 1037–1064.
1089 https://doi.org/10.1002/2017JD027445
1090

Figure 1.

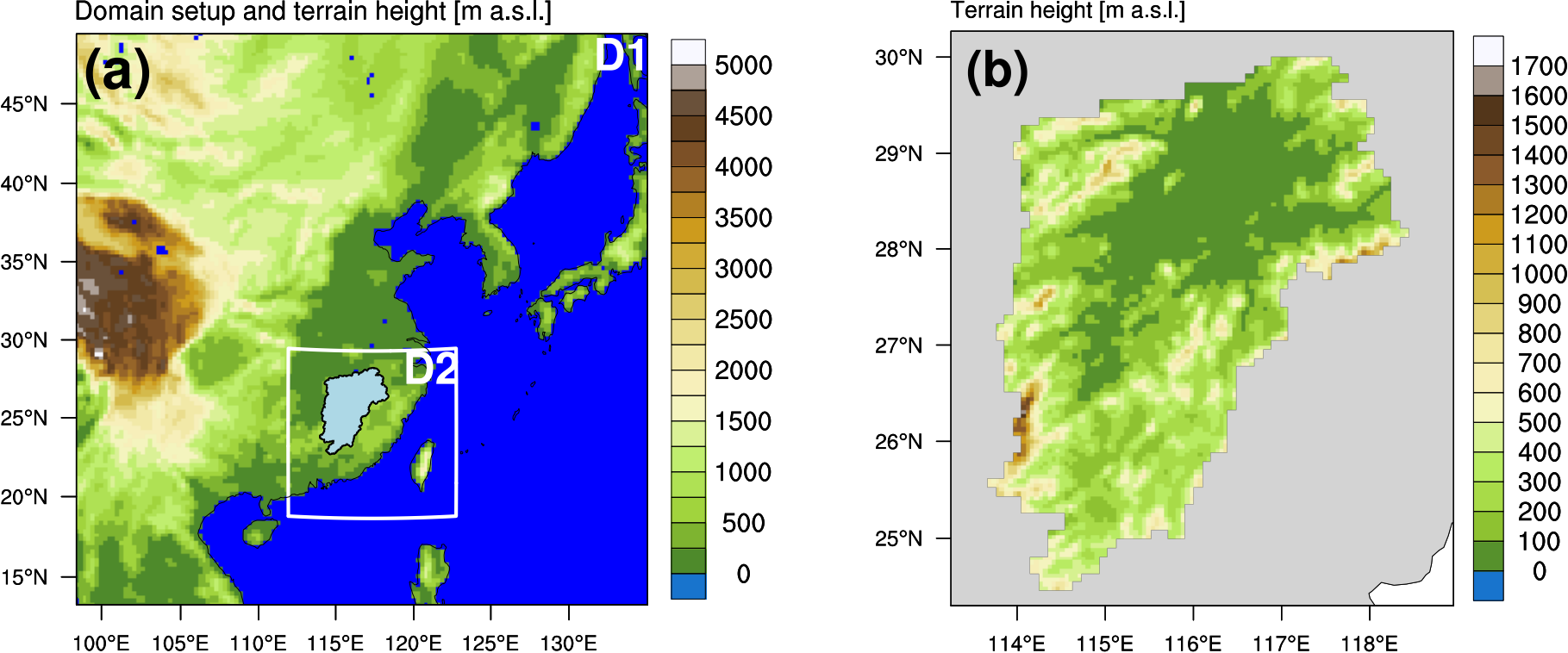
Domain setup and terrain height [m a.s.l.]
(a)
D1
D2
45°N
40°N
35°N
30°N
25°N
20°N
15°N
100°E
105°E
110°E
115°E
120°E
125°E
130°E
5000
4500
4000
3500
3000
2500
2000
1500
1000
500
0
Terrain height [m a.s.l.]
(b)
30°N
29°N
28°N
27°N
26°N
25°N
114°E
115°E
116°E
117°E
118°E
1700
1600
1500
1400
1300
1200
1100
1000
900
800
700
600
500
400
300
200
100
0

Figure 2.

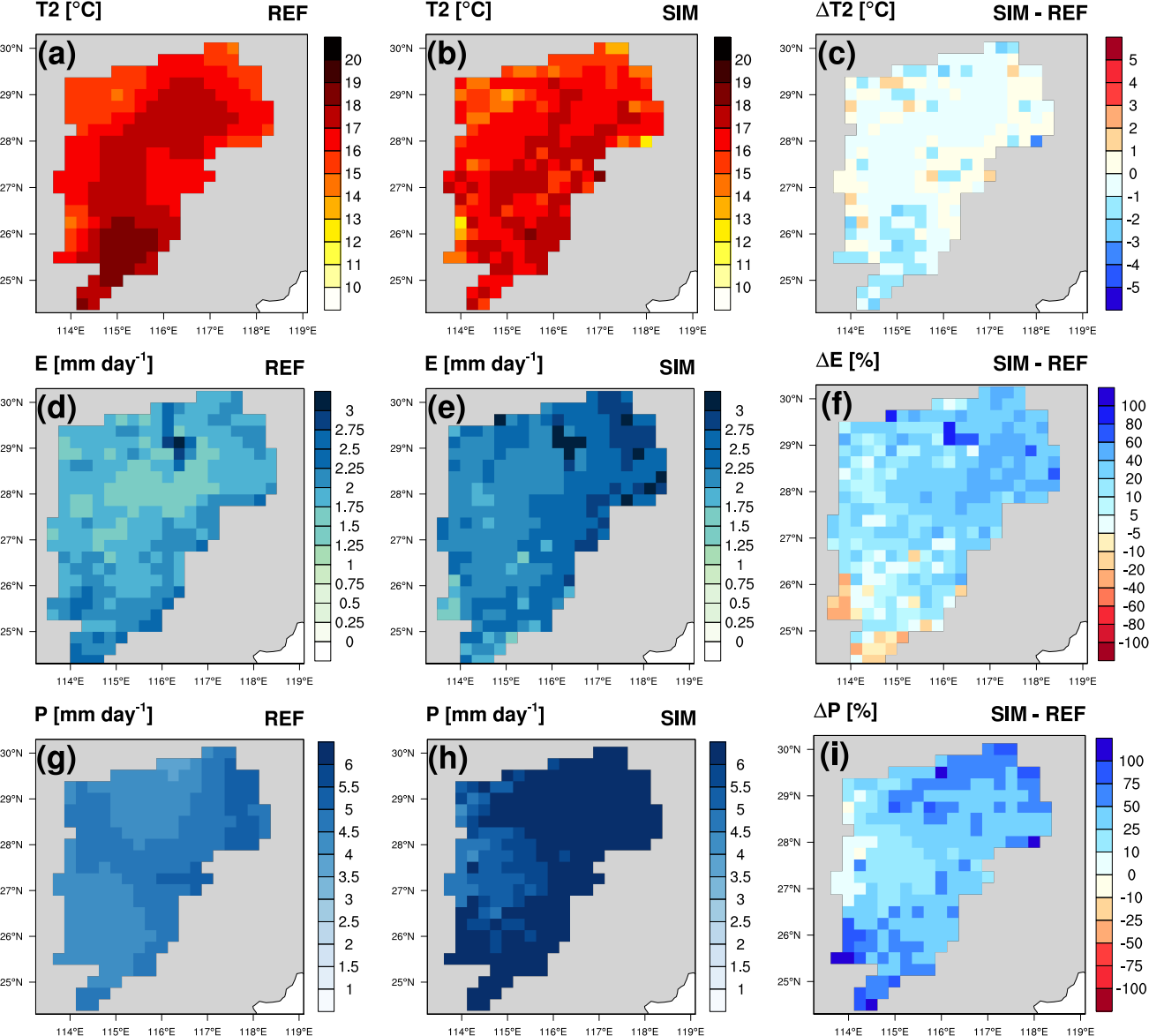
T2 [°C]
REF
(a)
T2 [°C]
SIM
(b)
ΔT2 [°C]
SIM - REF
(c)
E [mm day-1]
REF
(d)
E [mm day-1]
SIM
(e)
ΔE [%]
SIM - REF
(f)
P [mm day-1]
REF
(g)
P [mm day-1]
SIM
(h)
ΔP [%]
SIM - REF
(i)
30°N
29°N
28°N
27°N
26°N
25°N
114°E
115°E
116°E
117°E
118°E
119°E

Figure 3.

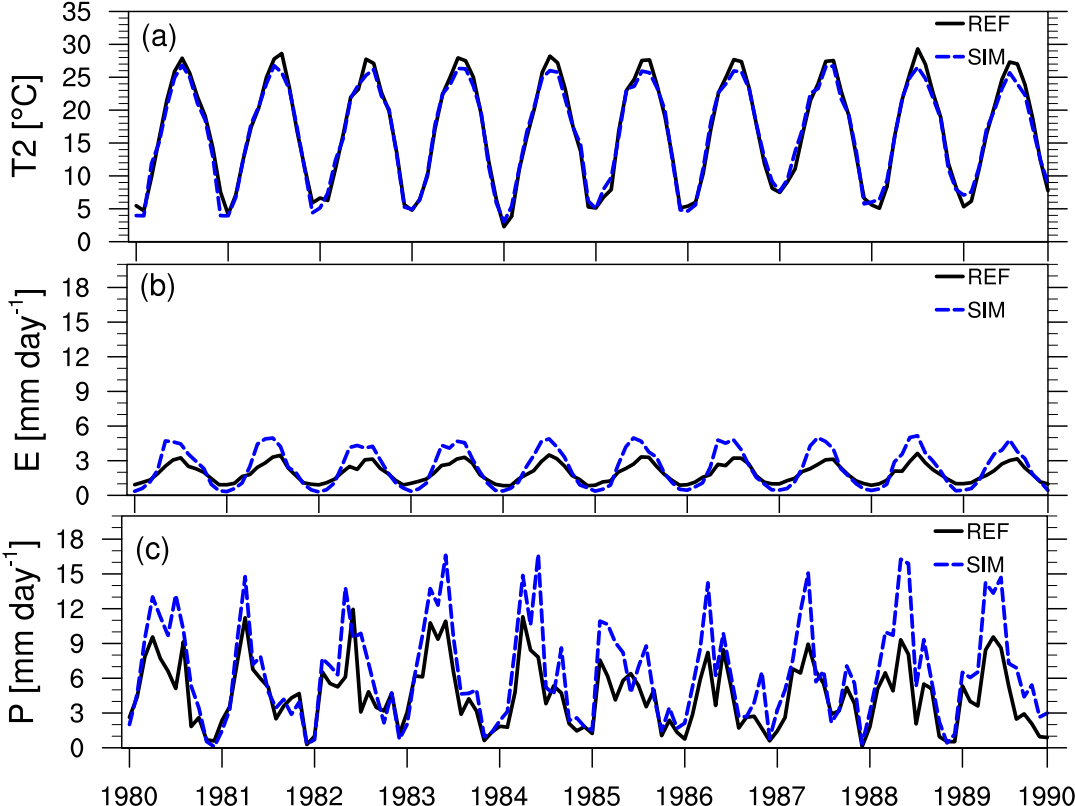
(a)
REF
SIM
T2 [°C]
35
30
25
20
15
10
5
0
(b)
REF
SIM
E [mm day-1]
18
15
12
9
6
3
0
(c)
REF
SIM
P [mm day-1]
18
15
12
9
6
3
0
1980
1981
1982
1983
1984
1985
1986
1987
1988
1989
1990

Figure 4.

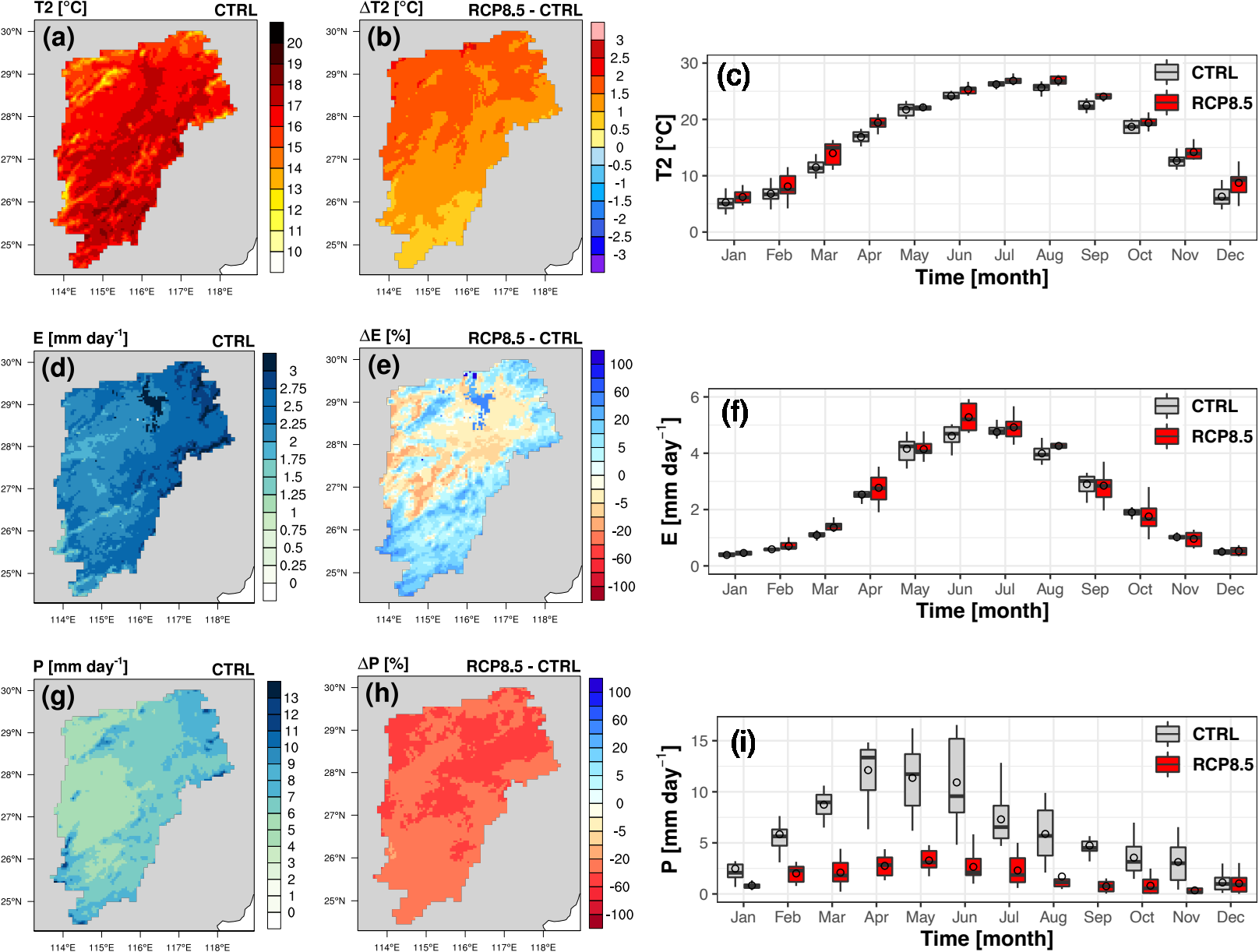
T2 [°C]
CTRL
(a)
ΔT2 [°C]
RCP8.5 - CTRL
(b)
(c)
CTRL
RCP8.5
T2 [°C]
Time [month]
E [mm day-1]
CTRL
(d)
ΔE [%]
RCP8.5 - CTRL
(e)
(f)
CTRL
RCP8.5
E [mm day-1]
Time [month]
P [mm day-1]
CTRL
(g)
ΔP [%]
RCP8.5 - CTRL
(h)
(i)
CTRL
RCP8.5
P [mm day-1]
Time [month]
Jan Feb Mar Apr May Jun Jul Aug Sep Oct Nov Dec
114°E 115°E 116°E 117°E 118°E
25°N 26°N 27°N 28°N 29°N 30°N

Figure 5.

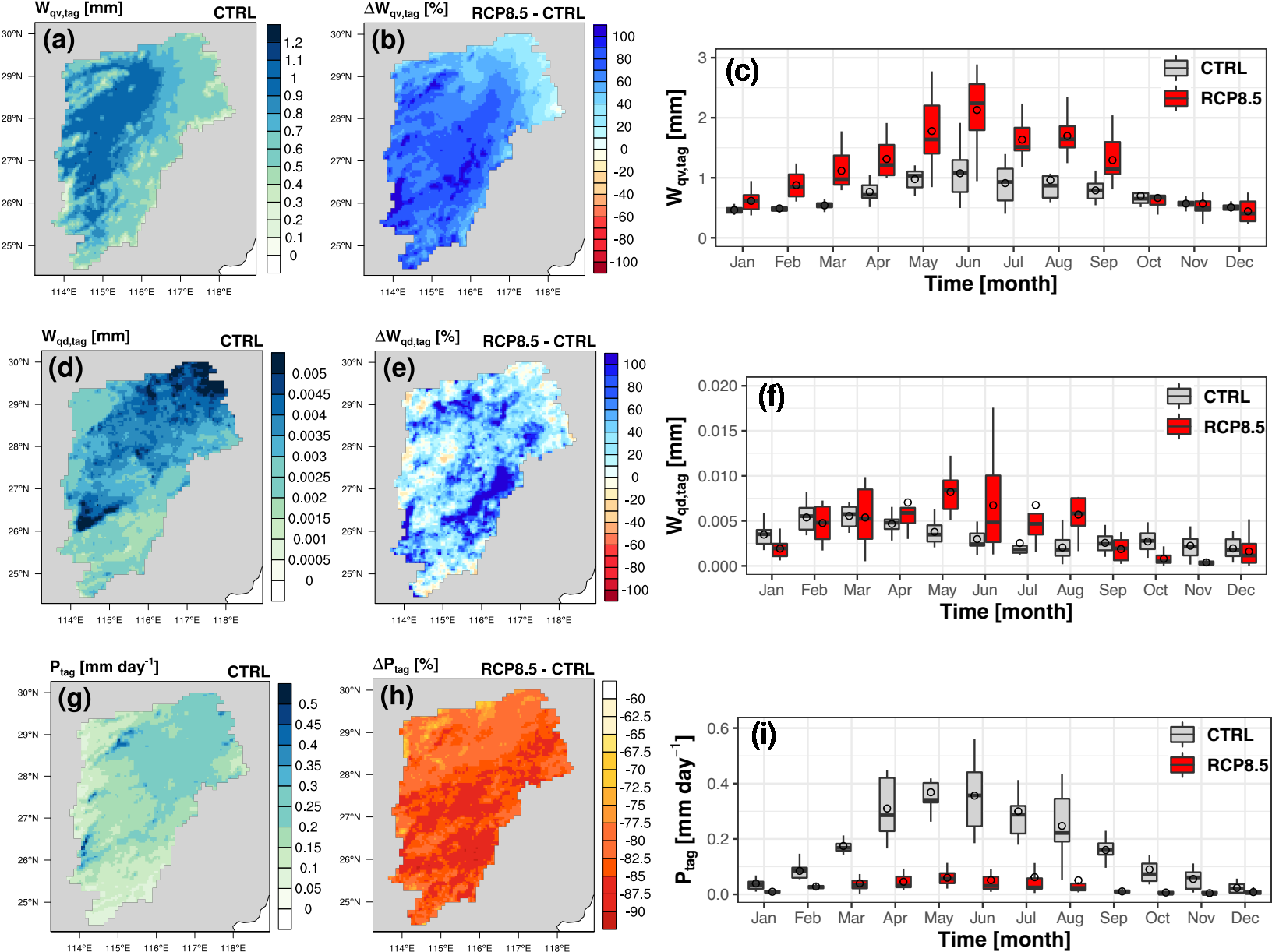
(a)
$W_{qv,tag}$ [mm]
CTRL
(b)
$\Delta W_{qv,tag}$ [%]
RCP8.5 - CTRL
(c)
$W_{qv,tag}$ [mm]
Time [month]
CTRL
RCP8.5
(d)
$W_{qd,tag}$ [mm]
CTRL
(e)
$\Delta W_{qd,tag}$ [%]
RCP8.5 - CTRL
(f)
$W_{qd,tag}$ [mm]
Time [month]
CTRL
RCP8.5
(g)
P_{tag} [mm day^{-1}]
CTRL
(h)
ΔP_{tag} [%]
RCP8.5 - CTRL
(i)
P_{tag} [mm day^{-1}]
Time [month]
CTRL
RCP8.5
Jan Feb Mar Apr May Jun Jul Aug Sep Oct Nov Dec
114°E 115°E 116°E 117°E 118°E
25°N 26°N 27°N 28°N 29°N 30°N

Figure 6.

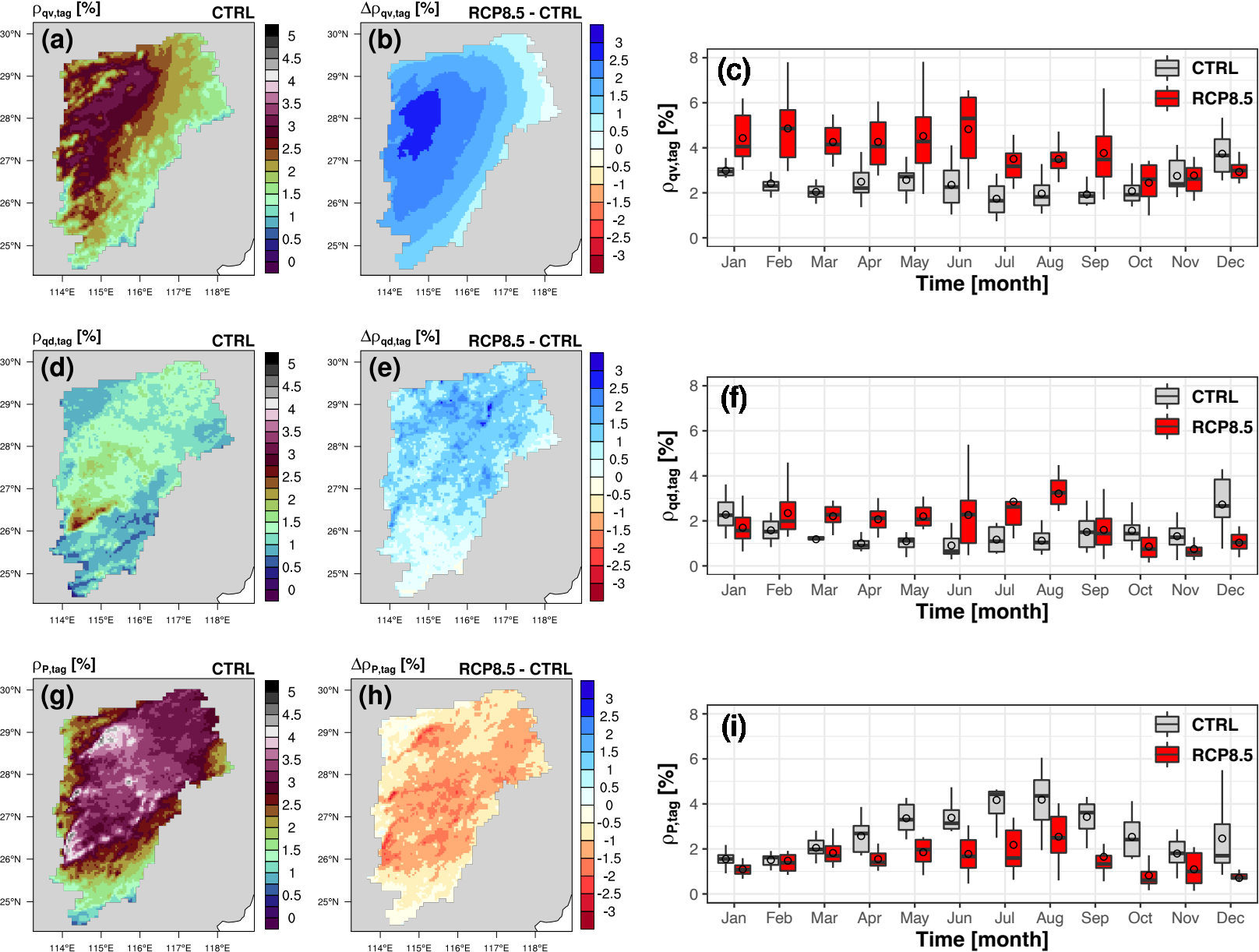
ρqv,tag [%]
CTRL
(a)
Δρqv,tag [%]
RCP8.5 - CTRL
(b)
(c)
CTRL
RCP8.5
ρqv,tag [%]
Time [month]
ρqd,tag [%]
CTRL
(d)
Δρqd,tag [%]
RCP8.5 - CTRL
(e)
(f)
CTRL
RCP8.5
ρqd,tag [%]
Time [month]
ρP,tag [%]
CTRL
(g)
ΔρP,tag [%]
RCP8.5 - CTRL
(h)
(i)
CTRL
RCP8.5
ρP,tag [%]
Time [month]
30°N
29°N
28°N
27°N
26°N
25°N
114°E
115°E
116°E
117°E
118°E
Jan
Feb
Mar
Apr
May
Jun
Jul
Aug
Sep
Oct
Nov
Dec

Figure 7.

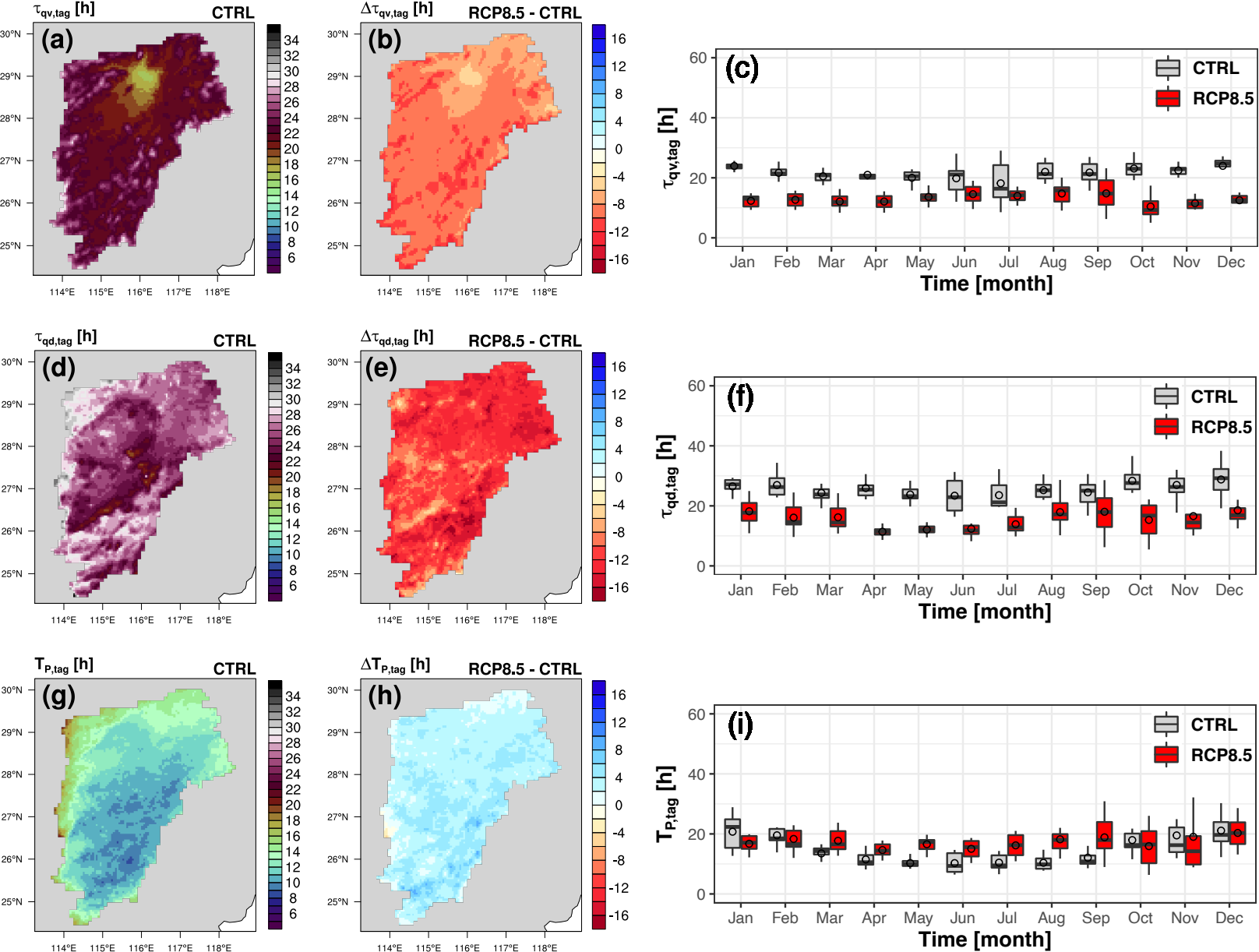
τqv,tag [h]
CTRL
(a)
Δτqv,tag [h]
RCP8.5 - CTRL
(b)
(c)
CTRL
RCP8.5
τqv,tag [h]
Time [month]
τqd,tag [h]
CTRL
(d)
Δτqd,tag [h]
RCP8.5 - CTRL
(e)
(f)
CTRL
RCP8.5
τqd,tag [h]
Time [month]
TP,tag [h]
CTRL
(g)
ΔTP,tag [h]
RCP8.5 - CTRL
(h)
(i)
CTRL
RCP8.5
TP,tag [h]
Time [month]
30°N
29°N
28°N
27°N
26°N
25°N
114°E
115°E
116°E
117°E
118°E
Jan
Feb
Mar
Apr
May
Jun
Jul
Aug
Sep
Oct
Nov
Dec

Figure 8.

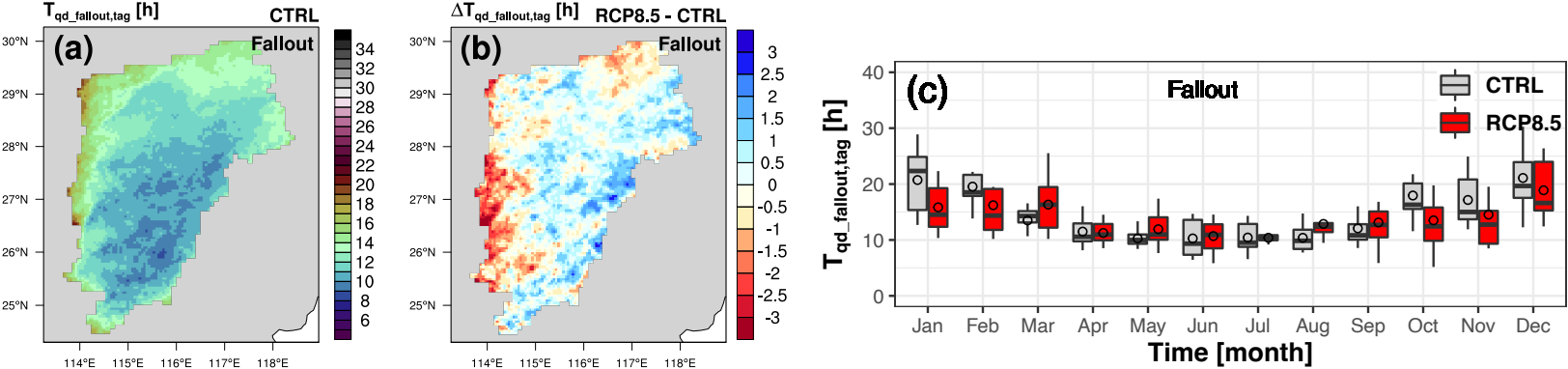
$T_{qd\_fallout,tag}$ [h]
CTRL
(a)
Fallout
30°N
29°N
28°N
27°N
26°N
25°N
114°E
115°E
116°E
117°E
118°E
34
32
30
28
26
24
22
20
18
16
14
12
10
8
6
$\Delta T_{qd\_fallout,tag}$ [h]
RCP8.5 - CTRL
(b)
Fallout
3
2.5
2
1.5
1
0.5
0
-0.5
-1
-1.5
-2
-2.5
-3
(c)
Fallout
CTRL
RCP8.5
$T_{qd\_fallout,tag}$ [h]
40
30
20
10
0
Jan
Feb
Mar
Apr
May
Jun
Jul
Aug
Sep
Oct
Nov
Dec
Time [month]

Figure captions

Figure 1. (a) Model domain setup: the 30 km outer (D1) and 5 km inner (D2) WRF simulation domains. The terrain heights (meters above sea level; m a.s.l.) of D1 and D2 are shown in color. The light blue shaded area, i.e., the Poyang Lake basin, marks the source where evaporated water is tagged and tracked using the WRF-age model. (b) Terrain height (m a.s.l.) of the investigated Poyang Lake basin.

Figure 2. Spatial distributions of the reference datasets (REF, left column) and the simulated (SIM, middle column) 2-meter air temperature *T2* in °C (first row), evaporation *E* in mm day^{-1} (second row), and precipitation *P* in mm day^{-1} (third row), averaged for the period 1980-1989. The right column shows the corresponding differences between the simulation and the reference datasets (SIM - REF).

Figure 3. Temporal variations of the basin-averaged 2-meter air temperature *T2* (°C), evaporation *E* (mm day^{-1}), and precipitation *P* (mm day^{-1}) from the reference datasets (REF, black solid line) and the simulation (SIM, blue dashed line) for the period from 1980 to 1989.

Figure 4. Spatial distributions of (first row) the simulated 2-meter air temperature *T2* in °C, (second row) evaporation *E* in mm day^{-1}, and (third row) precipitation *P* in mm day^{-1} over the Poyang Lake basin, averaged for (left column) the historical period 1980-1989 derived from the CTRL simulation. Middle column shows the differences $\Delta T2$ (°C), ΔE (%), and ΔP (%) between the future (2040-2049) RCP8.5 simulation and the historical CTRL simulation. The right column shows the boxplots of monthly variations of the basin-averaged *T2* in °C, *E* in mm day^{-1}, and *P* in mm day^{-1} from the historical CTRL (in gray) and future RCP8.5 (in red) simulations. The horizonal black solid lines and the black circles indicate medium and mean, respectively. The upper and bottom bounds of the box denote the 75th and 25th percentiles, respectively. The upper and bottom whiskers stand for the 95th and 5th percentiles, respectively.

Figure 5. As in Figure 4, but for (top row) the column-integrated tagged water vapor $W_{qv,tag}$ (mm), (middle row) the column-integrated tagged condensed atmospheric moisture $W_{qd,tag}$ (mm), and (bottom row) the tagged precipitation P_{tag} (mm day^{-1}).

Figure 6. As in Figure 4, but for the contribution ratios for (top row) the column-integrated tagged water vapor $\boldsymbol{\rho_{qv,tag}}$ (%), (middle row) the column-integrated tagged condensed atmospheric moisture $\boldsymbol{\rho_{qd,tag}}$ (%), and (bottom row) the tagged precipitation $\boldsymbol{\rho_{P,tag}}$ (%).

Figure 7. As in Figure 4, but for the atmospheric residence times of (top row) the column-integrated tagged water vapor $\boldsymbol{\tau_{qv,tag}}$ (h) and (middle row) the column-integrated tagged condensed atmospheric moisture $\boldsymbol{\tau_{qd,tag}}$ (h), and (bottom row) the atmospheric transit time of the tagged precipitation $\boldsymbol{T_{P,tag}}$ (h).

Figure 8. As in Figure 4, but for the atmospheric transit time of the tagged precipitating water fallout $T_{qd\_fallout,tag}$ (h).

Table 1. Model configuration and physical schemes of the WRF-age model used in this study.

Domain name	D1	D2
	Model configuration	
Domain size (grid points)	141 × 141	247 × 247
Horizontal resolution (km)	30	5
Vertical discretization (levels)	38	38
Time step (s)	60	20
Boundary update	6-hour	3-hour
	Physical scheme	
Cumulus	BMJ	-
Shortwave radiation	Dudhia	
Longwave radiation	RRTM	
Microphysics	WSM5	
Land surface	NOAH	
Surface layer	Revised MM5 Monin-Obukhov scheme	
Planetary boundary layer	YSU	
Shallow convection	-	